arXiv:2111.11764v1 [astro-ph.HE] 23 Nov 2021

A fast radio burst source at a complex magnetised site in a barred galaxy

H. Xu[1,2,3],J. R. Niu[2], P. Chen[1,3], K. J. Lee[1,2]*, W. W. Zhu[2]†, S. Dong[1]‡, B. Zhang[4]§, J. C. Jiang[1,2,3], B. J. Wang[1,2,3], J. W. Xu[1,2,3], C. F. Zhang[1,2,3], H. Fu[5], A. V. Filippenko[6,7], E. W. Peng[3,1], D. J. Zhou[2], Y. K. Zhang[2], P. Wang[2], Y. Feng[2], Y. Li[8], T. G. Brink[6], D. Z. Li[9], W. Lu[10], Y. P. Yang[11], R. N. Caballero[1], C. Cai[12], M. Z. Chen[13], Z. G. Dai[14], S. G. Djorgovski[15], A. Esamdin[13], H. Q. Gan[2], P. Guhathakurta[16], J. L. Han[2], L. F. Hao[17], Y. X. Huang[17], P. Jiang[2], C. K. Li[12], D. Li[2,18],H. Li[2], X. Q. Li[12], Z. X. Li[17], Z. Y. Liu[13], R. Luo[19], Y. P. Men[20], C. H. Niu[2], W. X. Peng[12], L. Qian[2], L. M. Song[12], D. Stern[21], A. Stockton[22], J. H. Sun[2], F. Y. Wang[23], M. Wang[17], N. Wang[13], W. Y. Wang[3], X. F. Wu[8], S. Xiao[12], S. L. Xiong[12], Y. H. Xu[17], R. X. Xu[3,1,24], J. Yang[23], X. Yang[8], R. Yao[2], Q. B. Yi[12], Y. L. Yue[2], D. J. Yu[2], W. F. Yu[27], J. P. Yuan[13], B. B. Zhang[23,25], S. B. Zhang[8], S. N. Zhang[12], Y. Zhao[12], W. K. Zheng[6], Y. Zhu[2], J. H. Zou[26,23]

[1]*Kavli Institute for Astronomy and Astrophysics, Peking University, Beijing 100871, P. R. China*
[2]*National Astronomical Observatories, Chinese Academy of Sciences, Beijing 100101, P.R. China*
[3]*Department of Astronomy, Peking University, Beijing 100871, P. R. China*
[4]*Department of Physics and Astronomy, University of Nevada, Las Vegas, NV 89154, USA*
[5]*Department of Physics & Astronomy, University of Iowa, Iowa City, IA 52242, USA*
[6]*Department of Astronomy, University of California, Berkeley, CA 94720-3411, USA*
[7]*Miller Senior Fellow, Miller Institute for Basic Research in Science, University of California, Berkeley, CA 94720, USA*
[8]*Purple Mountain Observatory, Chinese Academy of Sciences, Nanjing 210008, P .R . China*
[9]*TAPIR, Walter Burke Institute for Theoretical Physics, Mail Code 350-17, Caltech, Pasadena, CA 91125, USA*
[10]*Department of Astrophysical Sciences, Princeton University, Princeton, NJ 08544, USA*
[11]*South-Western Institute For Astronomy Research, Yunnan University, Yunnan 650504, P. R. China*
[12]*Key laboratory of Particle Astrophysics,Institute of High Energy Physics, Chinese Academy of Sciences, Beijing 100049, P.R. China*
[13]*Xinjiang Astronomical Observatory, Chinese Academy of Sciences, Urumqi 830011, P. R. China*
[14]*University of Science and Technology of China, Anhui 230026, P. R. China.*
[15]*Division of Physics, Mathematics, and Astronomy, California Institute of Technology, Pasadena,*

*E-mail: kjlee@pku.edu.cn, orcid.org/0000-0002-1435-0883
†Email: zhuww@nao.cas.cn, orcid.org/0000-0001-5105-4058
‡Email: dongsubo@pku.edu.cn, orcid.org/0000-0002-1027-0990
§Email: zhang@physics.unlv.edu, orcid.org/0000-0002-9725-2524

CA 91125, USA.
[16] *UCO/Lick Observatory, Department of Astronomy & Astrophysics, University of California Santa Cruz, 1156 High Street, Santa Cruz, CA 95064, USA*
[17] *Yunnan Observatories, Chinese Academy of Sciences, Kunming 650216, P. R. China*
[18] *Guizhou Normal University, Guiyang 550001, P. R. China*
[19] *CSIRO Space and Astronomy, Epping, NSW 1710, Australia*
[20] *Max-Planck institut für Radioastronomie, Auf Dem Hügel, Bonn, 53121, Germany*
[21] *Jet Propulsion Laboratory, California Institute of Technology, 4800 Oak Grove Drive, Pasadena, CA 91109, USA*
[22] *Institute for Astronomy, University of Hawaii, Honolulu, HI 96822, USA*
[23] *School of Astronomy and Space Science, Nanjing University, Nanjing 210093, P. R. China*
[24] *State Key Laboratory of Nuclear Physics and Technology, School of Physics, Peking University, Beijing 100871, P. R. China*
[25] *Key Laboratory of Modern Astronomy and Astrophysics (Nanjing University), Ministry of Education, P. R. China*
[26] *College of Physics, Hebei Normal University, Shijiazhuang 050024, P. R. China*
[27] *Shanghai Astronomical Observatory,Chinese Academy of Sciences, Shanaghai 200030, P. R. China*

Fast radio bursts (FRBs) are highly dispersed radio bursts prevailing in the universe[1–3]. The recent detection of FRB 200428 from a Galactic magnetar[4–8] suggested that at least some FRBs originate from magnetars, but it is unclear whether the majority of cosmological FRBs, especially the actively repeating ones, are produced from the magnetar channel. Here we report the detection of 1863 polarised bursts from the repeating source FRB 20201124A[9] during a dedicated radio observational campaign of Five-hundred-meter Aperture Spherical radio Telescope (FAST). The large sample of radio bursts detected in 88 hr over 54 days indicate a significant, irregular, short-time variation of the Faraday rotation measure (RM) of the source during the first 36 days, followed by a constant RM during the later 18 days. Significant circular polarisation up to 75% was observed in a good fraction of bursts. Evidence suggests that some low-level circular polarisation originates from the conversion from linear polarisation during the propagation of the radio waves, but an intrinsic radiation mechanism is required to produce the higher degree of circular polarisation. All of these features provide evidence for a more complicated, dynamically evolving, magnetised immediate environment around this FRB source. Its host galaxy was previously known[10–12]. Our optical observations reveal that it is a Milky-Way-sized, metal-rich, barred-spiral galaxy at redshift $z = 0.09795 \pm 0.00003$**, with the FRB source residing in a low stellar density, interarm region**

at an intermediate galactocentric distance, an environment not directly expected for a young magnetar formed during an extreme explosion of a massive star.

Triggered by observations of the Canadian Hydrogen Intensity Mapping Experiment (CHIME)[9], we used the FAST[13] to monitor FRB 20201124A from 2021 April 1 to June 11 (UT dates are used throughout this paper) with a 96.9 hr total observation time. The 19-beam receiver was used to cover the frequency range from 1.0 GHz to 1.5 GHz. From 2021 April 1 to April 2, we performed a grid of 9 observations using all 19 beams around the position ($\alpha = 05^{\rm h}08^{\rm m}$, $\delta = +26^\circ11'$) reported by the CHIME team[9] and detected multiple bursts in 2 to 4 beams simultaneously. We then used the differential intensity in each beam to compute a refined location[14], which agrees with the position measured by the European Very Long Baseline Interferometry Network (EVN) team [15]. Our later observation was carried out nearly daily by pointing the FAST central beam at the EVN position ($\alpha = 05^{\rm h}08^{\rm m}03.507^{\rm s}$, $\delta = +26^\circ03'38.50''$).

In total, 1863 bursts were detected with a signal-to-noise ratio $S/N > 7$, among which 913 bright bursts reach $S/N > 50$. The burst flux ranges from 0.005 to 11.5 Jy, and the inferred isotropic luminosity spans 5×10^{37} erg s^{-1} to 3×10^{40} erg s^{-1}. The daily luminosity distributions show little evolution during our observations (Figure 1), while pulse-to-pulse isotropic luminosities fluctuate by more than two orders of magnitude. The daily event rate evolved slowly from a minimal value of $5.6^{+0.9}_{-1.1}$ hr^{-1} to a maximal value of $45.8^{+7.8}_{-8.2}$ hr^{-1}, making FRB 20201124A among the most active FRBs known so far. During our monitoring program, we witnessed the sudden quenching of burst activity, when the source stopped emitting any bursts above the flux limit of 4.3 mJy at a fiducial pulse width of 5 ms on 2021 May 29. Before this abrupt cessation of emission, the burst event rate did not show any sign of a monotonic decrease. We continued to observe the source over the next 16 days and did not detected any single burst during the 9 hr of observations (Figure 1).

The polarisation properties of FRB 20201124A show a great diversity. Even though most bursts exhibit a flat polarisation angle (PA) across each burst, similar to FRB 20121102A[16], some bursts show significant PA swings similar to the case of FRB 20180301A[17]. Interestingly, FRB 20201124A had shown a high degree of circular polarisation in a good fraction of bursts, with a maximal percentage of 75%. This is in contrast to most FRBs[1] or radio-emitting magnetars[18] which do not show significant circular polarisation. One possible way of generating circular polarisation in FRBs is through the Faraday conversion mechanism[19,20], which rotates the linear and circular polarisation on the Poincaré sphere. We therefore searched for evidence of Faraday conversion in our data. For some bursts with moderate circular polarisation, the frequency spectra of both circular polarisation and linear polarisation indeed show clear oscillating structures (e.g., bursts 779 and 926 in Figure 2). The oscillation phases of the linear and circular polarisation are approximately offset by

$180^{\rm o}$. All of these are consistent with the Faraday conversion theory, suggesting that Faraday conversion is indeed one mechanism for producing circular polarisation in FRBs. On the other hand, we also detected highly circularly polarised bursts that lack quasiperiodic structures (e.g., burst 1472 in Figure 2). This suggests that there must be an intrinsic physical mechanism for producing circular polarisation other than Faraday conversion. Since circular polarisation is commonly observed in pulsar radio emission that has a magnetospheric origin, and since the synchrotron maser model invoking relativistic shocks does not predict circular polarisation, our results again offer support for a magnetospheric origin of FRB emission[3,17,21,22].

We monitored the evolution of the RM of FRB 20201124A, which shows a significant, irregular temporal variation from $-887.2 \pm +0.7$ to $-362.7^{+2.9}_{-1.4}\,{\rm rad\,m^{-2}}$ on a timescale of months (see Figure 1 and details in Methods). A pulse-to-pulse RM variation with a root-mean-square (RMS) value of $75.2\,{\rm rad\,m^{-2}}$ is also detected. Similar to pulsar observations, we note that the apparent RM value changing by $\sim 15.6\,{\rm rad\,m^{-2}}$ across a single pulse is allowed owing to profile evolution. No significant dispersion measure (DM) variation is detected with a 95% confidence level upper limit of $\Delta{\rm DM} \leq 2.9\,{\rm cm^{-3}\,pc}$. The RM variation suddenly stopped ~ 20 days before the quenching of radio bursts, while the event rate slowly increased from $5.6^{+0.9}_{-1.1}\,{\rm hr^{-1}}$ to $27.2^{+6.7}_{-7.5}\,{\rm hr^{-1}}$.

We measured the daily burst rate together with a shape parameter using the Weibul distribution. The shape parameter, with fluctuations, is generally smaller than 1 (Figure 1). Thus, the bursts tend to cluster compared to a Poisson distribution where no correlation is expected among bursts. The logarithmic waiting time follows a bimodal distribution with timescales peaking at 39 ms and 135.2 s (see Methods). Using the Lomb-Scargle periodogram algorithm, we can exclude periodicity from 30 ms to 10 days at the 95% confidence level.

We measured the scintillation bandwidth from the autocorrelation of the dynamic spectra. The measured scintillation bandwidth ($\sim 0.7\,{\rm MHz}$) agrees with previously reported values[23]. A pulse-to-pulse fluctuation of scintillation bandwidth with an RMS of 3 MHz is detected, but no systematic evolution of scintillation bandwidth is detected yet. Owing to the limited frequency coverage, we cannot exclude the possibility that such variation resulted from temporal evolution of the pulse profile.

We performed optical and near-infrared observations of the galaxy SDSS J050803.48+260338.0 identified as the FRB host[10–12] using the 10 m Keck telescopes. We took high- and low-dispersion spectra with the Echellette Spectrograph Imager (ESI) and the Low Resolution Imaging Spectrometer (LRIS), respectively, on 2021 April 7, g- and i-band images with LRIS on 2021 April 13, and K'-band images with the NIRC2 camera using the laser guide-star adaptive-optics (AO) system on 2021 August 17. We detected multiple emission lines (Figure 3(a)) and derive a precise redshift

$z = 0.09795 \pm 0.00003$, which corresponds to a luminosity distance of 453.3 ± 0.1 Mpc (or an angular size distance of 376.0 ± 0.1 Mpc) adopting the standard *Planck* cosmological model[24]. Similar to the hosts of several other repeaters (e.g., FRB 20121102A[25], FRB 20180916B[26], FRB 20180301A[27]), this host is in the star-forming branch of the Baldwin-Phillips-Terlevich (BPT) diagram [28] (Extended Data Figure 8(a)). Our AO image (Figure 3(b)) with a full width at half-maximum intensity (FWHM) resolution of 0.12", shows that the host is a barred galaxy with apparent spiral features, and the FRB's apparent location is in the disk but offset from the bar and spiral arms. The galaxy's stellar mass[10,11], $M_* \approx 3 \times 10^{10}\, M_\odot$, is about half as massive as the Milky Way (MW), which is also a barred spiral galaxy; in contrast, we find that its star-formation rate ($\mathrm{SFR} = 3.4 \pm 0.3\, M_\odot\, \mathrm{yr}^{-1}$) is about twice of that of MW, and its metallicity ($12 + \log(\mathrm{O/H}) = 9.07^{+0.03}_{-0.04}$) is approximately twice the solar abundance (see Methods). As shown in Extended Data Figure 8(b), the projected offset of the FRB location from the galaxy center and the specific SFR appear to be typical compared with known FRB hosts, and its metallicity is higher than that of any FRB host reported previously[29,30].

We also identify another galaxy at $z = 0.5534 \pm 0.0001$ with multiple emission lines detected in our spectra. The centroid of the background galaxy, which is measured using its [O III] emission line detected at two slit orientations, is separated by 0.36" from the foreground galaxy's center and 0.72" from the FRB. If the background galaxy were the FRB host, it would have a large projected separation of 4.7 kpc, and this scenario is disfavoured by the constraint imposed by the FRB's DM (see Methods). The close proximity of the two galaxies raises the curious possibility of gravitational lensing, since their separation is comparable to the angular Einstein radius of ~ 0.2", but more data are needed to verify this.

The large sample of radio bursts and the peculiar polarisation properties offer clues to the origin of this repeating FRB. If the central engine is an isolated young magnetar, the RM is predicted to show a secular monotonic decline with time, as the pulsar wind nebula expands[31,32]. The short-term RM evolution is not straightforwardly expected. Rather, it points toward a dynamically evolving, magnetised immediate environment around this FRB. One can place some interesting constraints on the magnetic field strength based on observations. First, the significant evolution of $|\mathrm{RM}|$ and the nondetection of DM evolution places a lower limit of $B > 0.1$ mG in the FRB environment (see Methods). Next, in the cold plasma limit the magnetic field of Faraday conversion may be estimated[20] using $B \sim 7 (\Pi_{\mathrm{V0}}/0.1)\, (\mathrm{RM}'/1000\, \mathrm{rad\, m^{-2}})^{-1/2}\, (\lambda/21\, \mathrm{cm})^{-2}$ G, where the oscillation amplitude (Π_{V0}) and the RM up to the Faraday conversion position (RM') are defined in Methods. The estimated magnetic field in the Faraday conversion medium is much higher than previously estimated for FRB 20121102A[19].

The month-timescale, significant RM variation could be caused by a change of either the

magnetic field configuration or density profile along the line of sight close to the source region. One may estimate the characteristic size of the Faraday screen as $\sim 0.2\ \mathrm{AU}(\tau/\mathrm{month})(v/10\ \mathrm{km\ s^{-1}})$, with τ and v being the timescale of RM variation and relative transverse velocity of the Faraday screen and the FRB source, respectively. The relative motion between the source and screen could be due to binary motion or proper motion of the source neutron star. The lack of periodicity may not rule out the binary scenario, since a known Galactic binary pulsar system also shows irregular RM evolution, probably related to irregular mass ejection from the companion star[33]. The cessation of RM variation in a later part of the observing window suggests that the line of sight is less contaminated by the varying component of the medium density.

The repeater FRB 20121102A is hosted by a metal-poor dwarf galaxy with high specific SFR[25]. These properties resemble those of the typical hosts for long-duration gamma-ray bursts (LGRBs) and hydrogen-poor superluminous supernovae (SLSNe-I), motivating a hypothesized connection between repeater FRBs and young, millisecond magnetars[34]. In contrast, the host of FRB 20201124A is more metal-rich and massive than almost all known hosts of LGRBs/SLSNe-I [30], and the location of the FRB does not coincide with an apparent active star-forming region in the host, so the hypothesis that the source is a young magnetar born during an extreme explosion such as an LGRB or an SLSN-I is not supported. A regular magnetar similar to those in the MW is still possible, but special conditions are needed to interpret the high FRB burst rate not possessed by Galactic magnetars.

1. Petroff, E., Hessels, J. W. T. & Lorimer, D. R. Fast radio bursts. Astron. Astrophys. Rev. **27**, 4 (2019).

2. Cordes, J. M. & Chatterjee, S. Fast Radio Bursts: An Extragalactic Enigma. Ann. Rev. Astron. Astrophys. **57**, 417–465 (2019).

3. Zhang, B. The physical mechanisms of fast radio bursts. Nature **587**, 45–53 (2020).

4. CHIME/FRB Collaboration et al. A bright millisecond-duration radio burst from a Galactic magnetar. Nature **587**, 54–58 (2020).

5. Bochenek, C. D. et al. A fast radio burst associated with a Galactic magnetar. Nature **587**, 59–62 (2020).

6. Li, C. K. et al. HXMT identification of a non-thermal X-ray burst from SGR J1935+2154 and with FRB 200428. Nature Astronomy **5**, 378 (2021).

7. Ridnaia, A. et al. A peculiar hard X-ray counterpart of a Galactic fast radio burst. Nature Astronomy **5**, 372–377 (2021).

8. Mereghetti, S. et al. INTEGRAL Discovery of a Burst with Associated Radio Emission from the Magnetar SGR 1935+2154. Astrophys. J. Lett. **898**, L29 (2020).

9. Chime/Frb Collabortion. Recent high activity from a repeating Fast Radio Burst discovered by CHIME/FRB. The Astronomer's Telegram **14497**, 1 (2021).

10. Fong, W.-f. et al. Chronicling the Host Galaxy Properties of the Remarkable Repeating FRB 20201124A. Astrophys. J. Lett. **919**, L23 (2021).

11. Ravi, V. et al. The host galaxy and persistent radio counterpart of FRB 20201124A. arXiv e-prints arXiv:2106.09710 (2021).

12. Piro, L. et al. The Fast Radio Burst FRB 20201124A in a star forming region: constraints to the progenitor and multiwavelength counterparts. arXiv e-prints arXiv:2107.14339 (2021).

13. Jiang, P. et al. Commissioning progress of the FAST. Sci. China Phys. Mech. Astron. **62**, 959502 (2019).

14. Xu, H. et al. FAST detection and localization of FRB20201124A. The Astronomer's Telegram **14518**, 1 (2021).

15. Nimmo, K. et al. Milliarcsecond localisation of the repeating FRB 20201124A. arXiv e-prints arXiv:2111.01600 (2021).

16. Michilli, D. et al. An extreme magneto-ionic environment associated with the fast radio burst source FRB 121102. Nature **553**, 182–185 (2018).

17. Luo, R. et al. Diverse polarization angle swings from a repeating fast radio burst source. Nature **586**, 693–696 (2020).

18. Kramer, M., Stappers, B. W., Jessner, A., Lyne, A. G. & Jordan, C. A. Polarized radio emission from a magnetar. Mon. Not. R. Astron. Soc. **377**, 107–119 (2007).

19. Vedantham, H. K. & Ravi, V. Faraday conversion and magneto-ionic variations in fast radio bursts. Mon. Not. R. Astron. Soc. **485**, L78–L82 (2019).

20. Gruzinov, A. & Levin, Y. Conversion Measure of Faraday Rotation-Conversion with Application to Fast Radio Bursts. Astrophys. J. **876**, 74 (2019).

21. Kumar, P., Lu, W. & Bhattacharya, M. Fast radio burst source properties and curvature radiation model. Mon. Not. R. Astron. Soc. **468**, 2726–2739 (2017).

22. Yang, Y.-P. & Zhang, B. Bunching Coherent Curvature Radiation in Three-dimensional Magnetic Field Geometry: Application to Pulsars and Fast Radio Bursts. Astrophys. J. **868**, 31 (2018).

23. Main, R. A. et al. Scintillation timescale measurement of the highly active FRB20201124A. arXiv e-prints arXiv:2108.00052 (2021).

24. Planck Collaboration et al. Planck 2015 results. XIII. Cosmological parameters. Astron. & Astrophys. **594**, A13 (2016).

25. Chatterjee, S. et al. A direct localization of a fast radio burst and its host. Nature **541**, 58–61 (2017).

26. Marcote, B. et al. A repeating fast radio burst source localized to a nearby spiral galaxy. Nature **577**, 190–194 (2020).

27. Bhandari, S. et al. Characterizing the FRB host galaxy population and its connection to transients in the local and extragalactic Universe. arXiv e-prints arXiv:2108.01282 (2021).

28. Baldwin, J. A., Phillips, M. M. & Terlevich, R. Classification parameters for the emission-line spectra of extragalactic objects. Publ. Astron. Soc. Pac. **93**, 5–19 (1981).

29. Bhandari, S. et al. The Host Galaxies and Progenitors of Fast Radio Bursts Localized with the Australian Square Kilometre Array Pathfinder. Astrophys. J. Lett. **895**, L37 (2020).

30. Li, Y. & Zhang, B. A Comparative Study of Host Galaxy Properties between Fast Radio Bursts and Stellar Transients. Astrophys. J. Lett. **899**, L6 (2020).

31. Piro, A. L. & Gaensler, B. M. The Dispersion and Rotation Measure of Supernova Remnants and Magnetized Stellar Winds: Application to Fast Radio Bursts. Astrophys. J. **861**, 150 (2018).

32. Metzger, B. D., Margalit, B. & Sironi, L. Fast radio bursts as synchrotron maser emission from decelerating relativistic blast waves. Mon. Not. R. Astron. Soc. **485**, 4091–4106 (2019).

33. Johnston, S., Ball, L., Wang, N. & Manchester, R. N. Radio observations of PSR B1259-63 through the 2004 periastron passage. Mon. Not. R. Astron. Soc. **358**, 1069–1075 (2005).

34. Metzger, B. D., Berger, E. & Margalit, B. Millisecond Magnetar Birth Connects FRB 121102 to Superluminous Supernovae and Long-duration Gamma-Ray Bursts. Astrophys. J. **841**, 14 (2017).

Figure 1:**Overview of our radio observational campaign and temporal variations of the physical parameters for FRB 20201124A.** (a) Daily number of bursts detected. (b) and (c) Event rate and Weibull shape parameter (k). (d) and (e) Degree of linear and circular polarisation components measured for each individual burst. (f) Daily number of bursts showing the Faraday conversion feature. (g), (h), and (i) Daily RM, DM, and burst energy, where the violin symbol indicates the distribution function, the green shaded strip indicate the 95% upper and lower bounds, and the solid black curve is the median. (j) The observation length of each day. The grey shaded region on the right side of the plot shows the epoch when no bursts were detected.

Figure 2:**Polarisation profiles, dynamic spectra, degree of polarisation, and spectra of bandpass of selected bursts** (a) PA curve with 95% confidence level error bars. (b) Polarisation pulse profile, where total intensity, linear, and circular polarisation normalised to the off-pulse noise of total intensity are in black, red, and blue curves, respectively. (c) Dynamic spectra of total intensity. The horizontal white strips and red markers represent frequency channels that have been removed owing to either radio frequency interference (RFI) or band edges. (d) Total intensity. (e) Degree of polarisation as a function of the square of wavelength, where green, magenta, and blue dots and error bars are for total, linear, and circular polarisation, respectively. The solid curves of the corresponding colour are the model fitting excluding data in the grey region (see Methods). The phase difference between the linear and circular polarisation is denoted. (f) Lomb-Scargle spectra of (e), where the horizontal dashed line indicates the 95% confidence level. The best Bayesian RM value is used to derotate the linear PA. The pulse number is given in panel (a). Four bursts are selected to show the following properties. Burst 779: flat PA, low degree of circular polarisation, but showing oscillation in polarisation for λ^2 smaller than 0.07 m^2 (frequency lower than 1160 MHz). Burst 926: similar to burst 779, but the Faraday conversion oscillation is detected across the full signal bandwidth. Burst 1112: swinging PA, high degree of circular polarisation, shows slow variation in polarisation across frequency. Burst 1472: pulse with the largest degree of circular polarisation, swinging PA.

Figure 3:**Host properties at optical and near-infrared wavelengths.** (a) Emission lines from the $z = 0.098$ (black) and $z = 0.553$ (yellow) galaxies in the LRIS (blue) and ESI (red) spectra, with regions contaminated by Earth's atmosphere marked in green. (b) The left sub-panel shows the K'-band AO image of the barred spiral galaxy at $z = 0.098$, with the indicated positions of the FRB[15] (cyan) and the centroid of the $z = 0.553$ galaxy (yellow star); the latter is determined using the [O III] emission from the two-dimensional (2D) spectroscopic images of ESI (upper right) and LRIS (lower right), respectively. We first constrain the [O III] centroid to be on the dashed lines (red, ESI; blue, LRIS) shown in the left sub-panel, by using their relative offsets from the continuum centers marked with dotted lines in both the upper-right and lower-right panels. It is

then pinned down by taking advantage of the different orientations of the LRIS and ESI slits (solid lines).

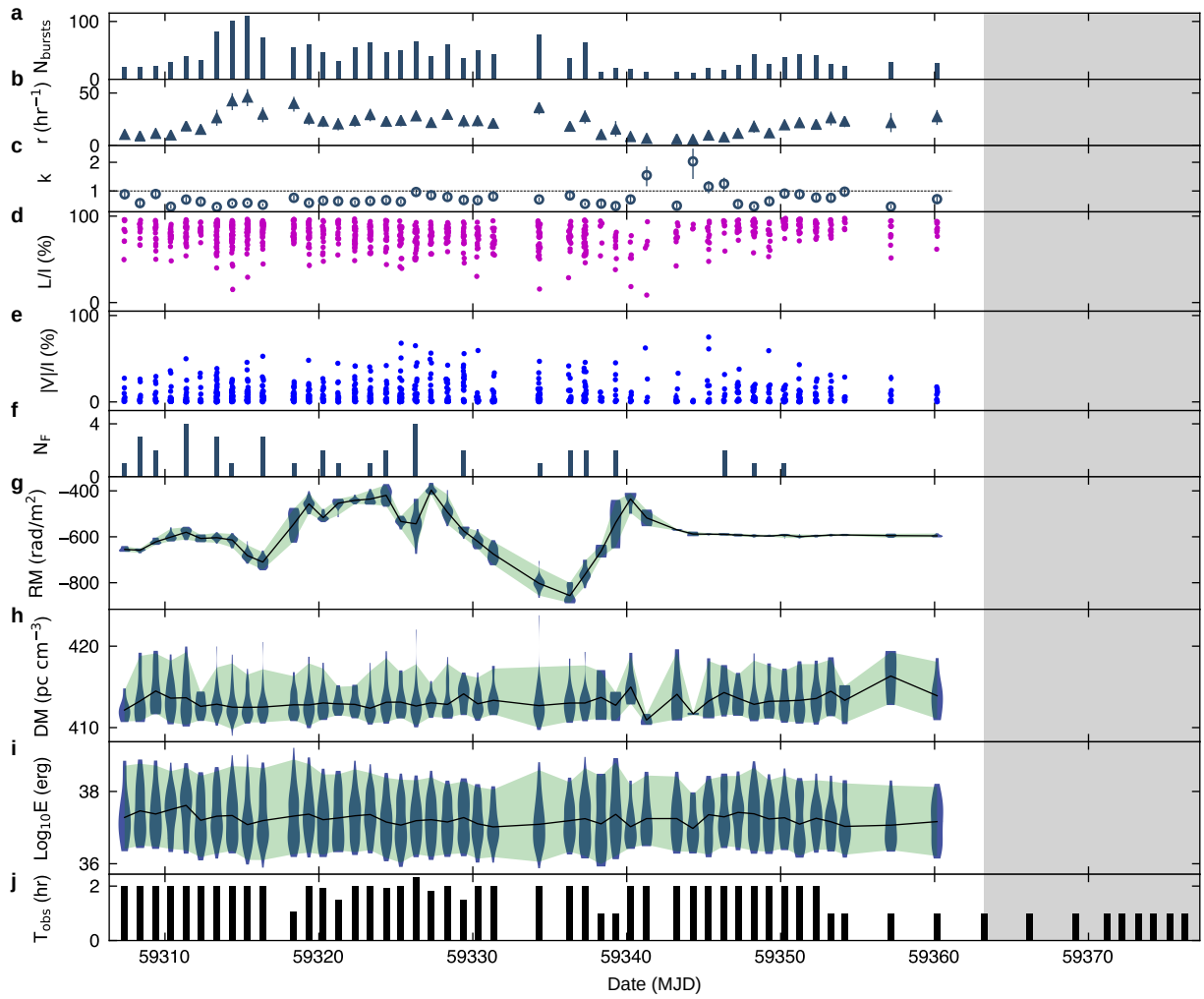

Figure 1: **Overview of our radio observational campaign and temporal variations of the physical parameters for FRB 20201124A.** (a) Daily number of bursts detected. (b) and (c) Event rate and Weibull shape parameter (k). (d) and (e) Degree of linear and circular polarisation components measured for each individual burst. (f) Daily number of bursts showing the Faraday conversion feature. (g), (h), and (i) Daily RM, DM, and burst energy, where the violin symbol indicates the distribution function, the green shaded strip indicate the 95% upper and lower bounds, and the solid black curve is the median. (j) The observation length of each day. The grey shaded region on the right side of the plot shows the epoch when no burst was detected.

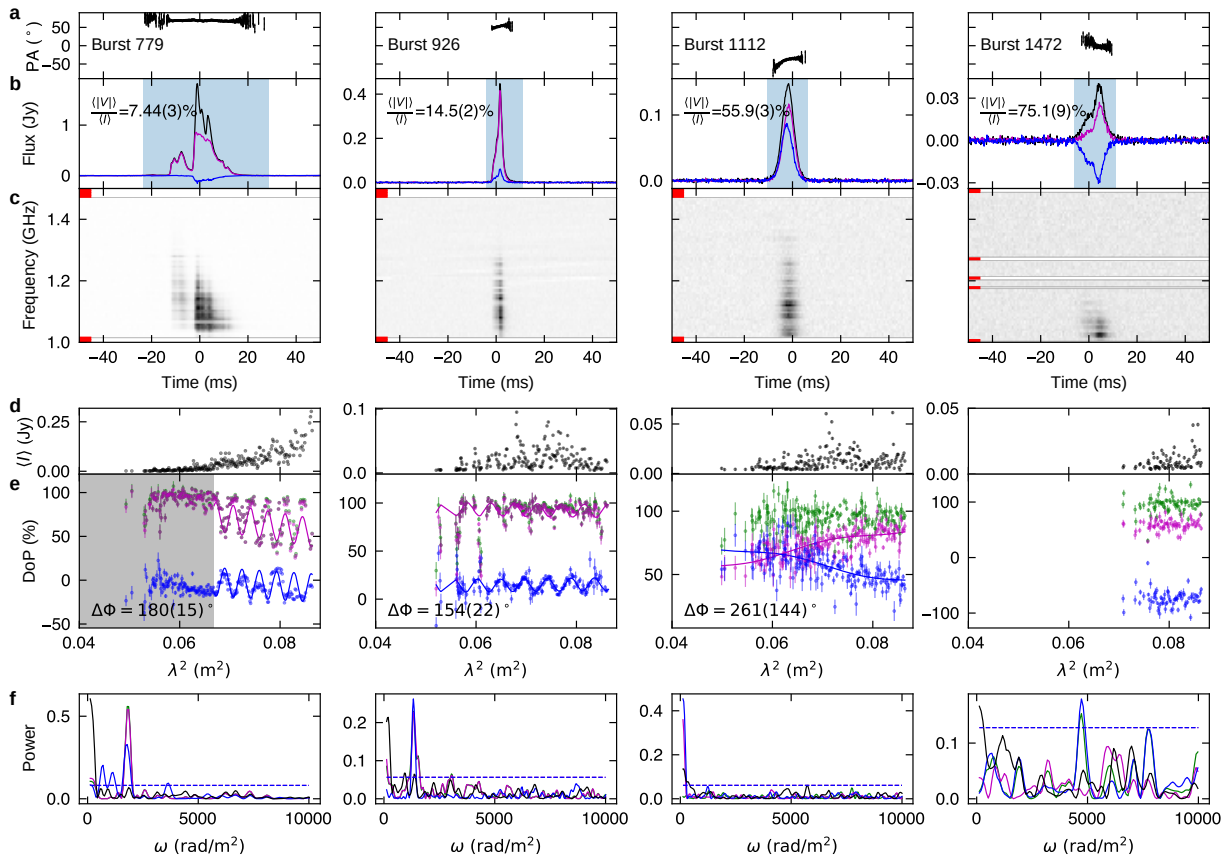

Figure 2: **Polarisation profiles, dynamic spectra, degree of polarisation, and spectra of band-pass of selected bursts** (a) PA curve with 95% confidence level error bars. (b) Polarisation pulse profile, where total intensity, linear, and circular polarisation normalised to the off-pulse noise of total intensity are in black, red, and blue curves, respectively. (c) Dynamic spectra of total intensity. The horizontal white strips and red markers represent frequency channels that have been removed owing to either radio frequency interference (RFI) or band edges. (d) Total intensity. (e) Degree of polarisation as a function of the square of wavelength, where green, magenta, and blue dots and error bars are for total, linear, and circular polarisation, respectively. The solid curves of the corresponding colour are the model fitting excluding data in the grey region (see Methods). The phase difference between the linear and circular polarisation is denoted. (f) Lomb-Scargle spectra of (e), where the horizontal dashed line indicates the 95% confidence level. The best Bayesian RM value is used to derotate the linear PA. The pulse number is given in panel (a). Four bursts are selected to show the following properties. Burst 779: flat PA, low degree of circular polarisation, but showing oscillation in polarisation for λ^2 smaller than 0.07 m^2 (frequency lower than 1160 MHz). Burst 926: similar to burst 779, but the Faraday conversion oscillation is detected across the full signal bandwidth. Burst 1112: swinging PA, high degree of circular polarisation, shows slow variation in polarisation across frequency. Burst 1472: pulse with the largest degree of circular polarisation, swinging PA.

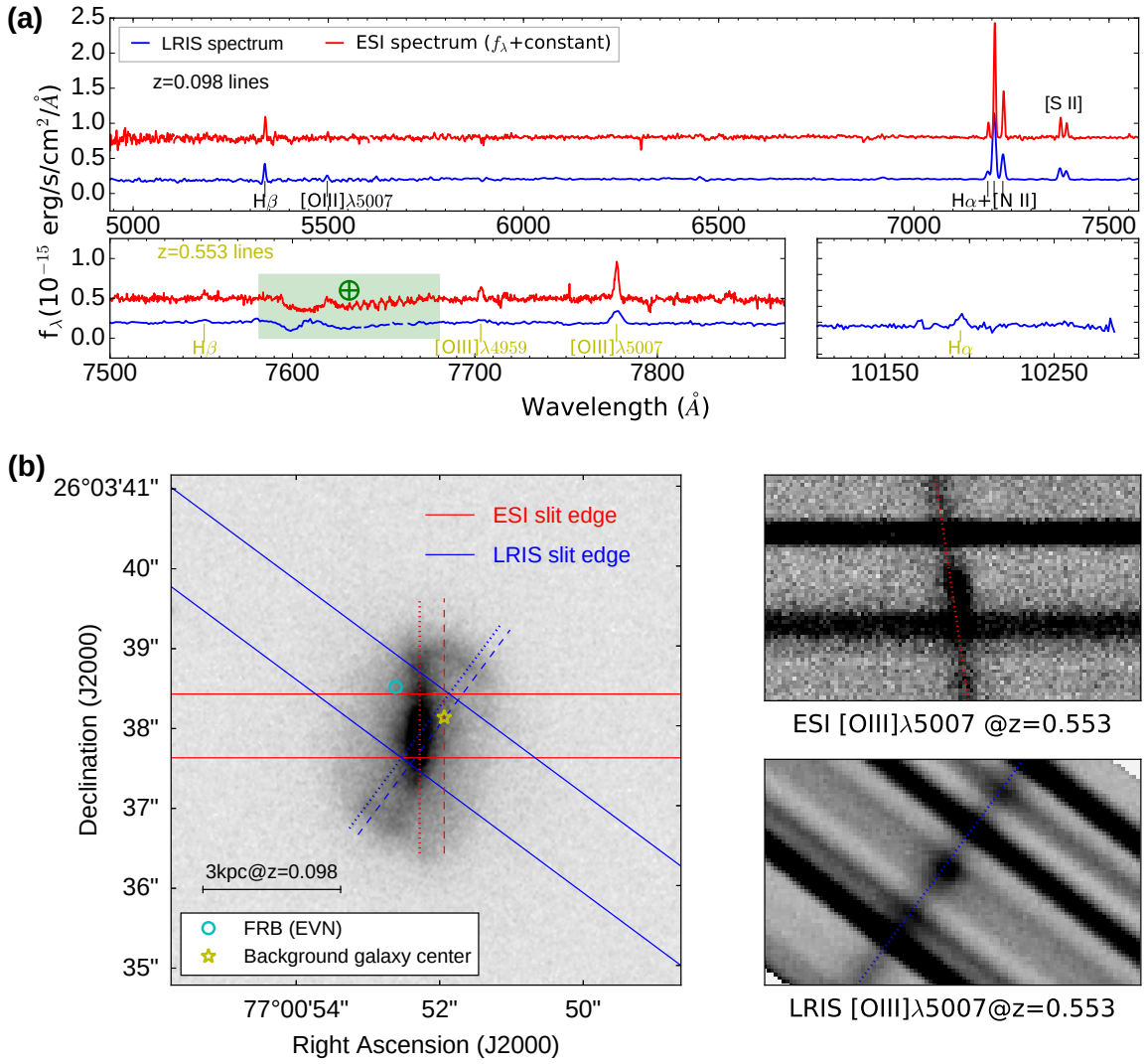

Figure 3: **Host properties at optical and near-infrared wavelengths.** (a) Emission lines from the $z = 0.098$ (black) and $z = 0.553$ (yellow) galaxies in the LRIS (blue) and ESI (red) spectra, with regions contaminated by Earth's atmosphere marked in green. (b) The left sub-panel shows the K'-band AO image of the barred spiral galaxy at $z = 0.098$, with the indicated positions of the FRB[15] (cyan) and the centroid of the $z = 0.553$ galaxy (yellow star); the latter is determined using the [O III] emission from the two-dimensional (2D) spectroscopic images of ESI (upper right) and LRIS (lower right), respectively. We first constrain the [O III] centroid to be on the dashed lines (red, ESI; blue, LRIS) shown in the left sub-panel, by using their relative offsets from the continuum centers marked with dotted lines in both the upper-right and lower-right panels. It is then pinned down by taking advantage of the different orientations of the LRIS and ESI slits (solid lines).

Methods

Radio observations and burst detection

We started our observations using the 19-beam receiver of FAST on 2021 April 1, which was triggered by the CHIME alarm [9]. The 19-beam receiver spans from 1.0 GHz to 1.5 GHz with a system temperature of 20–25 K [35]. During the April 1 and 2 observations, we performed a grid observation of FRB 20201124, where 9 pointings around the position reported by CHIME[9] were used to cover the $28' \times 35'$ area around the source. After the source was localised, we used the central beam and continued observing the source since April 3. The epochs and durations of all observations are shown in Figure 1. The data of April 1 and 2 were used only for localisation purposes[14]; they are excluded in other analyses in this paper, as the beam center was not aligned with the source position.

The data were recorded with a frequency resolution of 122.07 kHz and a temporal resolution of 49.152 μs or 196.608 μs. The full polarisation 4-channel Stokes intensity is derived with the linear polarisation feed[35]. Before and after each observation session, we recorded a 1 min noise calibrator signal for the purpose of polarisation calibration.

We used the software TRANSIENTX[1] to perform the off-line burst searches. For FRB 20201124A, the data were dedispersed in the range of 380–440 $\mathrm{cm}^{-3}\,\mathrm{pc}$ with a step of 0.1 $\mathrm{cm}^{-3}\,\mathrm{pc}$ and the pulse width was searched with a boxcar filter, of which the pulsar width ranges from 0.1 ms to 100 ms. After candidate plots were formed, we visually inspected all candidates with $S/N \geq 7$. A total of 1863 bursts were detected in our observations; the detected numbers of bursts for each observation session are plotted in Figure 1. We also verified the search results using the software BEAR[36]. No difference can be found for bursts with $S/N \geq 7$.

Event-rate evolution and the sudden quenching

We adopted the Weibull distribution[37] to describe the probability density of time intervals between bursts. The Weibull distribution of time interval δ is

$$W(\delta|k,r) = k\delta^{-1}[\delta\, r\Gamma(1+1/k)]^k e^{-[\delta\, r\Gamma(1+1/k)]^k}, \tag{1}$$

where the Gamma function is defined as $\Gamma(x) \equiv \int_0^\infty t^{x-1}\mathrm{e}^{-t}\mathrm{d}t$, r is the expected event rate, and k is the shape parameter. When $k = 1$, the Weibull distribution reduces to the Poisson distribution and burst events are independent of each other. When burst events tend to cluster together, the shape parameter $k < 1$.

[1] https://github.com/ypmen/TransientX

The statistical inferences for the parameters r and k were carried out using a Bayesian method based on the likelihood described by Oppermann et al.[37]. The software package MULTINEST[38] was used to perform posterior sampling. The event rate and shape parameter inferred with daily data are shown in panels (c) and (d) in Figure 1. For most of the observations we have $k < 1$, which indicates that the bursts tend to cluster together. With all the data, the inferred average event rate and shape parameter are $r = 20.5 \pm 1.6\,\mathrm{hr}^{-1}$ and $k = 0.60 \pm 0.02$ for a 95% confidence level.

As shown in Figure 1, the burst rate increased from $10.3^{+2.3}_{-2.8}\,\mathrm{hr}^{-1}$ to $45.8^{+7.8}_{-8.3}\,\mathrm{hr}^{-1}$ from April 3 (MJD 59307) to April 11 (MJD 59315), and then decreased to a 14-day plateau with an average rate of $27.0^{+1.6}_{-1.5}\,\mathrm{hr}^{-1}$. The event rate gradually decreased to a low of $5.6^{+0.9}_{-1.1}\,\mathrm{hr}^{-1}$ until May 10 (MJD 59344), and slowly returned to a plateau of $17.8^{+6.0}_{-5.6}\,\mathrm{hr}^{-1}$ on May 14 (59348). On May 29 (MJD 59363), the FRB source was suddenly quenched. No more bursts were detected with $S/N \geq 7$ thereafter in 20 days with a total of 9 hr observations, during which the corresponding 95% confidence level event rate upper limit is $\leq 0.3\,\mathrm{hr}^{-1}$.

Flux, fluence, and energy of bursts

We estimated the flux densities (S) through the radiometer equation

$$S = \frac{(S/N) \cdot T_{\rm sys}}{G\sqrt{2\mathrm{BW}\, t_{\rm samp}}}, \tag{2}$$

where the digitisation correction is neglected owing to the 8-bit sampling scheme at FAST[39], $T_{\rm sys} \approx 20$ K, and $G \approx 16\,\mathrm{K\,Jy}^{-1}$ are the typical system temperature and telescope gain for FAST[35], $t_{\rm samp}$ is the sampling time, and S/N is the signal-to-noise ratio. BW is the bandwidth of the burst derived from the Gaussian fitting method[40]. The dominant uncertainty ($\sim 20\%$) in flux-density estimation comes from the variation of system temperature[35].

Our pulse fluence (F) was computed by integrating the pulse flux with respect to time, while the equivalent width $W_{\rm eq}$ was computed by dividing the fluence by the pulse peak flux. The distributions of fluence and equivalent width are shown in Extended Data Figure 1. The average and the RMS deviation of the equivalent width are 7.6 ms and 3.3 ms, while the average fluence and its RMS are 0.5 Jy ms and 1.0 Jy ms.

The sample completeness was determined with the following recipe. We simulated 10,000 mock FRB bursts. The mock bursts were simulated with a Gaussian profile and bandpass, where the pulse width and bandwidth of the injections were controlled to match the distributions of detected bursts. We then injected the mock bursts into the original FAST data when no FRB was detected. The injection epoch is random but follows a uniform distribution. The simulated data

were then fed to our burst-searching pipeline to compute the detection rate. Averaging over the pulse width and bandpass distributions, the fluence threshold to achieve the 95% detection rate with $S/N \geq 7$ is 53 mJy ms.

With the fluence, the isotropic burst energy E was calculated through

$$E = \frac{4\pi D_L^2}{1+z} F \, \mathrm{BW}, \tag{3}$$

where $D_L = 453.3 \pm 0.1$ Mpc is the luminosity distance computed with $z = 0.09795 \pm 0.00003$ and the standard *Planck* cosmological model[24], and F is the fluence. We obtained a population of energies for the 1863 bursts; the histogram of burst energies and the cumulative distribution function of the burst energy above a given threshold (i.e., $N(> E)$) are shown in Extended Data Figure 1.

Temporal aspects of the bursts

The burst times of arrival (TOAs) were measured from the centroid of the best-matched box-car filter[36], as the complex morphology of the pulse shape prevents us from using the standard template-matching technique [41]. We then converted the site arrival times to the barycentric arrival times using the software package TEMPO2[42].

The waiting times (ΔT_{wait}) were calculated by subtracting pairs of two adjacent barycentric TOAs within the same observing session. The distribution of the waiting time is shown in Extended Data Figure 2. One can find a clear bimodal distribution in the logarithmic waiting time. We modeled the distribution using the superposition of three log-normal distributions, where the best-fitting curve to the histogram is also shown in Extended Data Figure 2. The three individual distributions peak at 39 ms, 45.1 s, and 162.3 s. We note that the superposition of two log-normal distributions cannot describe the waiting-time distribution well (see Extended Data Figure 2), and the Kolmogorov-Smirnov test rejects the two-component model with a p-value of 2×10^{-5}. The bimodal distribution of waiting time is similar to the case of FRB 20121102A[43], where the three-component distributions peak at 3.4 ms, 70 s, and 220 s. We note that the shortest waiting-time population (39 ms) is one order of magnitude longer than that of FRB 20121102A (3.4 ms).

We searched for burst periodicity from FRB 20201124A using the Lomb-Scargle periodogram[44] in the range from 30 ms to 10 days, as shown in Extended Data Figure 3. No obvious period above the 95% confidence level is detected, except for the artificial period around 1 day and its harmonics induced by the observation cadence.

Scintillation and scattering

The dynamic spectra of FRB 20201124A show a complex morphology, such as frequency drifting, single/multiple components, and small-scale voids, similar to other cases[17,45–47]. We investigated scintillation and scattering only with the single-peak pulses, where the measurements were less affected by the pulse structure.

The scintillation bandwidth (i.e., decorrelation bandwidth) is the frequency range over which the pulse intensity falls to half its maximum value. We measured the scintillation bandwidth using the autocorrelation function (ACF) method[48]. The measurement was performed for selected pulses with $S/N \geq 50$. Our procedures is as follows. (1) Split the data into 8 evenly spaced subbands across the 500 MHz raw bandwidth; (2) clip channels RFI and 20 MHz band edges (i.e., 1.0–1.02 GHz and 1.48–1.5 GHz); (3) for each subband with $S/N \geq 10$, integrate the pulse intensities over time and then compute the ACFs along the frequency axis; (4) a Lorentzian function is fitted to the measured ACFs, and the half width at half-maximum intensity of the Lorentzian function is the decorrelation bandwidth of the given subband; and (5) a power-law function is fitted to the decorrelation bandwidth measured in subbands (i.e., $\mathrm{BW_{sc}} = \mathrm{BW_{sc,1\,GHz}}(\nu/1\,\mathrm{GHz})^{-\gamma}$, with ν being the central frequency of each subband and γ the power-law index). The power-law function fitting aids to compute $\mathrm{BW_{sc,1\,GHz}}$ (i.e., the decorrelation bandwidth with a reference frequency of 1 GHz). As seen *a posteriori*, the decorrelation bandwidth (~ 1 MHz) is two orders of magnitude smaller than the signal bandwidth (~ 100 MHz), the finite-sample error[49] can be neglected, and the dominant error comes from statistical errors or pulse intrinsic evolution.

The measured decorrelation bandwidth is summarised in Extended Data Figure 4. No visible long-term trend of decorrelatiton bandwidth variation is detected, but we cannot exclude the short-term fluctuations. The average and RMS values of decorrelation bandwidth are 0.7 MHz and 3.0 MHz (respectively), consistent with the previous result of ~ 0.5 MHz measured with wider frequency coverage[23] (dual bands of 650 MHz and 1.5 GHz). We note that the index γ (average value of 4.9) is fluctuating with an RMS of 6.4. Such a fluctuation in γ is a caution that our measurement for the correlation bandwidth may be affected by the FRB intrinsic radiation properties, and that multiband observations with a wider frequency coverage are required to reduce such systematics. The corresponding scattering timescale according to the scintillation bandwidth will be at the level of $1/0.7\,\mathrm{MHz} \approx 1.4\,\mu$s, which is much smaller than the pulse width or temporal resolution of our data.

Dispersion measure

Owing to the complex time-frequency structure of FRB pulses, the DM of an FRB is usually derived by maximising the structure or contrast instead of aligning the pulse centroid [45]. This can be done in the time domain[45] or the Fourier domain [40]. In this paper, we used the Fourier-domain method, where the DM is measured by maximising the time derivative of "intensity" computed only with the Fourier phase[2]. After the best DM value is computed, we dedisperse the pulses and perform visual inspection to verify that the pulse structure is aligned in the time domain.

The DM vales as a function of time are collected in Figure 1. Although there is a significant change (maximal fluctuation $\sim 10\,\mathrm{cm^{-3}\,pc}$) in the burst-to-burst DM, a linear fitting to the trend in DM variation produces no obvious DM variation rate with $\mathrm{d}\mathrm{DM}/\mathrm{d}t = -3(4) \times 10^{-3}\,\mathrm{cm^{-3}\,pc\,day^{-1}}$ (i.e., there seems to be little systematic evolution of DM). In total, the mean value is $413.2\,\mathrm{cm^{-3}\,pc}$ and the RMS deviation is $2.0\,\mathrm{cm^{-3}\,pc}$. Despite little long-term DM evolution, we note that the RMS of daily DM is not stationary. In particular, on May 7 (MJD 59341) and May 10 (MJD 59344) the daily RMS of DM dropped by a factor of ~ 4 and ~ 14, as shown in Figure 1.

The measured DM agrees with our current understanding of the astronomical diffuse ionised medium. The major contributors to the FRB DM are (1) the Galactic medium ($\mathrm{DM_{MW}}$), (2) the Galactic halo ($\mathrm{DM_{halo}}$), (3) the intergalactic medium ($\mathrm{DM_{IGM}}$), and (4) the FRB host galaxy and local environment ($\mathrm{DM_{host}}/(1+z)$). FRB 20201124A is located close to the Galactic plane (longitude $l = 177.77°$, latitude $b = -8.52°$). The current Galactic electron density models predict a noticeable value of Galactic DM contribution toward this direction, with the NE2001 model[50] and the YMW16 model[51] predicting $\mathrm{DM_{MW}} \approx 140\,\mathrm{cm^{-3}\,pc}$ and $\mathrm{DM_{MW}} \approx 200\,\mathrm{cm^{-3}\,pc}$, respectively. The intergalactic medium contribution of a homogeneous ionised universe is $\mathrm{DM_{IGM}} = 80\,\mathrm{cm^{-3}\,pc}$ for $z = 0.09795$ (ref.[52]). Using the DM template technique [53] together with host galaxy parameters of Hα luminosity $L_{\mathrm{H}\alpha} = 7 \times 10^{41}\,\mathrm{erg\,s^{-1}}$ and effective radius $R_e = 1.5\,\mathrm{kpc}$ (see the section on optical observations), the predicted most probable host galaxy DM is $\mathrm{DM_{host}}/(1+z) = 60\,\mathrm{cm^{-3}\,pc}$ with a 68% confidence level range of $10 \leq \mathrm{DM_{host}}/(1+z) \leq 310\,\mathrm{cm^{-3}\,pc}$. Assuming a Galactic halo contribution of $30\,\mathrm{cm^{-3}\,pc}$ (ref.[54]), the expected DM of the FRB will be in the range of 260 to $620\,\mathrm{cm^{-3}\,pc}$, in agreement with the observed $\mathrm{DM} \approx 413\,\mathrm{cm^{-3}\,pc}$. Basing on the DM measurement, the background galaxy ($z = 0.5534$) is disfavoured as the FRB host, of which the expected $\mathrm{DM_{IGM}} = 660\,\mathrm{cm^{-3}\,pc}$ is already larger than the measured DM. However, the possibility cannot be fully ruled out, as a high anisotropy of the intergalactic medium may allow a low $\mathrm{DM_{IGM}}$ value along a particular line of sight.

[2] https://www.github.com/DanieleMichilli/DM_phase

Polarisation properties

Our polarisation data are calibrated with the single-axis model using the software package PSRCHIVE[55]. Both the differential gain and phase between the two polarisation channels are calibrated using noise diode signal injected in the feed. The polarisation fidelity and calibration scheme have been described and tested in previous work [17,35].

We measure the RM with bursts of $S/N \geq 30$ (1103 in total) using the Q–U fitting method[56]. Our curve fitting is carried out using a Bayesian method[56], where the posterior sampling is performed with the software package MULTINEST[38]. We corrected the ionosphere contribution with values computed from the software package IONFR[57]. For our data, the maximal ionosphere RM correction is $3\,\mathrm{rad\,m^{-2}}$.

The result of the measured RM (for an Earth observer) is shown in Figure 1. We note that the RM can have pulse-to-pulse fluctuations in daily observations; for example, the data taken on April 22 (MJD 59325) show the largest RM fluctuation with an RMS of $75.2\,\mathrm{rad\,m^{-2}}$. On top of the pulse-to-pulse fluctuations, one also observes significant RM evolution during the observing span. Previously, a long-term RM variation was reported in FRB 20121102A [58], where its RM value dropped by 34% over 2.6 yr. For FRB 20201124A, from April 23 (MJD 59327) to May 2 (MJD 59336), RM varied from -887.2 ± 0.7 to $-362.7^{+2.9}_{-1.4}\,\mathrm{rad\,m^{-2}}$, nearly a factor of two RM variation within 10 days. On a longer timescale, the RM variation is also different between FRB 20201124A and FRB 20121102A, with FRB 20201124A showing red-noise-like variations instead of a quasimonotonic decreasing trend as in the case of FRB 20121102A.

The RM variation on a monthly timescale cannot be explained with the RM contribution in the Milky Way, which is $-51(5)\,\mathrm{rad\,m^{-2}}$ along the direction of FRB 20201124A; the maximal variation is a few tens of radians per square meter[59]. Given the redshift $z = 0.09795 \pm 0.00003$ of the host galaxy (see Properties of the Foreground Galaxy part of Methods), RM in the source rest frame is $\mathrm{RM_{host}} = (1+z)^2(\mathrm{RM_{obs}} - \mathrm{RM_{Gal}}) = -380\,\mathrm{rad\,m^{-2}}$ to $-1010\,\mathrm{rad\,m^{-2}}$. Considering the monthly timescale of RM variation, we expect that the major RM variation comes from the FRB local environment, over a distance scale $\sim 100\ \mathrm{km\,s^{-1}} \times 1\ \mathrm{month} \approx 1.8\ \mathrm{au}$. Since no long-term DM variation is measured, we can derive a very conservative bound on the parallel magnetic field from $\langle B_\parallel \rangle \geq 1.23\ \mathrm{uG} \times \Delta\mathrm{RM_{Host}}/\Delta\mathrm{DM_{host}} \approx 0.1\mathrm{mG}$.

The RM variation is not caused by instrumental artifacts. In polarisation studies, we have excluded the data of April 1 and 2, where the observations were carried out with off-axis illumination. The FAST polarimetry stability has been checked[17] to show that the RM measurement is stable with $\Delta\mathrm{RM} \leq 0.2\,\mathrm{rad\,m^{-2}}$. Because of the high sensitivity of FAST, we also checked if

saturation or nonlinearity affected our polarimetry. The radio-frequency frontend of FAST has a dynamic range of ~ 30 dB with the major limitation introduced by the microwave-optical transducer (product model GL7430 of FOXCOM). The digital sampling and data recording is done with an 8-bit sampling scheme at FAST. Thus, the major nonlinearity comes from the digital part. We tested the nonlinearity by comparing the differences in results between including and removing the data above 250 (maximal digital value is 255 for an 8-bit system). The differences are tiny, so the results and conclusions of this paper are not affected.

As already noted in studies of pulsars[60] and FRBs[61], there is an apparent RM variation across the phase of a single pulse owing to the intrinsic frequency evolution of the pulse profile. We check if the RM variation of FRB 20201124A is induced by such an effect. We find that the maximum amplitude of RM variations within single pulses for FRB 20201124A is at the level of $15\,\mathrm{rad\,m^{-2}}$. Examples of the 9 brightest bursts are shown in Extended Data Figure 6. The long-term RM variation with an amplitude of $\sim 500\,\mathrm{rad\,m^{-2}}$ is much larger than the RM variation amplitude within single-pulse profiles; thus, it does not seem to be caused by the frequency evolution of the FRB pulse profile. We also checked if the rotation of linear polarisation agrees with the cold plasma Faraday rotation model. To do so, we relaxed the power-law index of wavelength and fit for the RM index β using the model $\Delta\Psi = \mathrm{RM}\,\lambda^{\beta}$. One expects $\beta = 2$ if the cold plasma Faraday rotation model can be applied, while the index β would not necessarily equal 2 if the apparent RM is caused by intrinsic profile evolution. As shown in Extended Data Figure 5, we found that for 83% bursts (920 out of 1103 bursts) the deviations of measured RM index values are within 1σ errorbars. Visual inspection revealed that the $\beta \neq 2$ deviation was mainly caused by overlapping of multiple components in the dynamic spectrum. The trend of RM variation is hardly affected by the small deviations as shown in Extended Data Figure 5, where one can see that the RM variation is very similar when including or removing the data with more than 1σ deviations of β from 2. The above tests indicate that the long-term RM variation is indeed caused by the cold plasma Faraday rotation. To further reduce the profile-evolution effects, only the measurements with RM index within 1σ of $\beta = 2$ are included in Figure 1.

We note that polarised emission dominates in the pulse of FRB 20201124A after correcting for Faraday rotation. In particular, 50% of the pulses have linear polarisation higher than 77.9% and circular polarisation higher than 3.3%. A low degree of polarisation is also detected, and the minimal linear and circular polarisation is 8.7% and below the detection threshold, respectively. On the one hand, we note that the circular polarisation is generally weaker than linear polarisation; 95% of the pulses have $V/I \leq 32.4\%$. On the other hand, certain pulses show a high degree of circular polarisation with a maximal value of 75.1% in the frequency-integrated profile (see pulse 1472 in Figure 2), which is rarely detected in other FRBs[2].

For a limited number of bursts, we have discovered a λ^2-dependent oscillation of circular and linear degrees of polarisation. The occurrence epochs of such bursts are indicated in Figure 1, with two examples (bursts 779 and 926) presented in Figure 2. We compute the Lomb-Scargle periodogram[44] for the degree of total, linear, and circular polarisation. With the technique, we find common peaks corresponding to the same conjugate frequency (ω_{λ^2}). We then perform a χ^2 fitting to the following model simultaneously for circular and linear polarisation intensity,

$$L = I\left[\Pi_{\rm L0} + \dot{\Pi}_{\rm L}\lambda^2 + A\sin(\omega_{\lambda^2}\lambda^2 + \phi_{\rm L})\right] , \quad (4)$$

$$V = I\left[\Pi_{\rm V0} + \dot{\Pi}_{\rm V}\lambda^2 + A\sin(\omega_{\lambda^2}\lambda^2 + \phi_{\rm V})]\right] , \quad (5)$$

where parameters $\Pi_{\rm L0}$, $\dot{\Pi}_{\rm L}$, $\Pi_{\rm V0}$, and $\dot{\Pi}_{\rm V}$ are the average value and slope of linear and circular degree of polarisation, respectively, while A and ω_{λ^2} are the amplitude and angular frequency of oscillation. Two independent phase parameters ($\phi_{\rm L}$ and $\phi_{\rm V}$) are introduced in the modeling, such that we can check the phase difference between the oscillation of $\Pi_{\rm L} \equiv L/I$ and $\Pi_{\rm V} \equiv V/I$. Here, we perform the fitting with polarisation intensity instead of directly fitting with degree of polarisation. This can be justified with the similar arguments in Q–U fitting[56]. The best fitting conjugate frequency of burst 779 and 926 are $\omega_{\lambda^2} = 2400 \pm 30\,{\rm rad\,m^{-2}}$ and $1800 \pm 10\,{\rm rad\,m^{-2}}$. In the framework of mild Faraday conversion, one have $|{\rm RM'}| = \omega_{\lambda^2}/2$, which is the Faraday rotation accumulated up to a given position where the conversion occurs. The total observed RM should be of the same order of magnitude. For such a scenario, this corresponds to ${\rm RM'} = 1200 \pm 15\,{\rm rad\,m^{-2}}$, $900 \pm 5\,{\rm rad\,m^{-2}}$, respectively.

We plot the best-fit curves against the data in Figure 2, where we convert the model to degree of polarisation for better visualisation. The best-fit phase differences between the linear and circular oscillations are given in panel (e) of Figure 2. For burst 779, the oscillation of $\Pi_{\rm V}$ and $\Pi_{\rm L}$ decrease significantly above 1160 MHz (indicated by the shaded area in Figure 2), where the best-fit amplitudes of oscillation below and above 1160 MHz are 0.16 ± 0.01 and 0.008 ± 0.005, respectively.

We checked the power index of oscillation with respect to λ by replacing terms of $\omega_{\lambda^2}\lambda^2$ in Eq. (4) and (5) to a generalised form of $\omega_{\lambda^{2k}}\lambda^{2k}$ and fit the index k simultaneously. For burst 779 and 926, we had $k = 0.998 \pm 0.005$ and 1.0 ± 0.1, which verifies the λ^2-dependent oscillation of polarisation degree.

As shown in Figure 2, the fitting model sinusoidal curves trace the variation of $\Pi_{\rm L}$ and $\Pi_{\rm V}$. The phase differences between the $\Pi_{\rm L}$ and $\Pi_{\rm V}$ curves are $\sim 180^\circ$. Such a phenomenon is in agreement with the prediction of Faraday conversion[20]. We note that the total degree of polarisation, $\Pi_{\rm P} \equiv \sqrt{L^2 + V^2}/I$, is also oscillating. Such behaviour was not explicitly claimed in

the papers addressing the Faraday conversion effects in the FRB context[19,20]. To fully understand the physics of the oscillating $\Pi_{\rm P}$, a complete modeling of polarisation transfer is required, which is beyond the scope of the current paper. Instead, we present a qualitative analysis. We caution that the discussion below can only apply to the local behaviour of radiation transfer.

Neglecting spontaneous emission, the radiative-transfer equation takes the form of[62,63]

$$\frac{d\mathbf{S}}{ds} = -\begin{pmatrix} \eta & \mu & 0 & \rho \\ \mu & \eta & -f & g \\ 0 & f & \eta & -h \\ \rho & -g & h & \eta \end{pmatrix} \mathbf{S}\,, \tag{6}$$

where the anti-Hermitian terms f describe Faraday rotation, g and h describe Faraday conversion, and the Hermitian terms μ, ρ, and η describe wave absorption or amplification. $\mathbf{S} = (I, Q, U, V)$ is the vector presentation of the Stokes parameters. We can write the components of the Stokes parameters as

$$\mathbf{S} = \begin{pmatrix} I \\ \Pi_{\rm L} I \cos\Phi \\ \Pi_{\rm L} I \sin\Phi \\ \Pi_{\rm V} I \end{pmatrix}\,, \tag{7}$$

with the initial Faraday rotation angle $\Phi = 2{\rm RM}'\lambda^2$. Substituting the above equations into Eq. (6), one can show that

$$\frac{d\Pi_{\rm V}}{ds} = (g + \mu\Pi_{\rm V})\Pi_{\rm L}\cos\Phi - h\Pi_{\rm L}\sin\Phi - \rho(1-\Pi_{\rm V}^2)\,, \tag{8}$$

$$\frac{d\Pi_{\rm L}}{ds} = -\left(g\Pi_{\rm V} + \mu(1-\Pi_{\rm L}^2)\right)\cos\Phi + h\Pi_{\rm V}\sin\Phi + \rho\Pi_{\rm L}\Pi_{\rm V}\,, \tag{9}$$

$$\frac{d\Pi_{\rm P}}{ds} = -\frac{\mu\Pi_{\rm L}}{\Pi_{\rm P}}\left(1-\Pi_{\rm P}^2\right)\cos\Phi - \frac{\rho\Pi_{\rm V}(1-\Pi_{\rm P}^2)}{\Pi_{\rm P}}\,. \tag{10}$$

We can see from the above equations that both the $\sin\Phi$ or $\cos\Phi$ terms induce the λ^2-dependent oscillation. In order to get the λ^2-dependent $\Pi_{\rm P}$, the Hermitian coefficient μ must be nonzero. Faraday conversion involves terms containing g and h. They introduce interactions between the linear and the circular polarisations, which are λ^2-dependent. To keep $\Pi_{\rm L}$ and $\Pi_{\rm P}$ in phase, we need (i) the term containing $\sin\Phi$ to be negligible compared with the terms containing $\cos\Phi$, and (ii) the same sign holds for the terms $g\Pi_{\rm V} + \mu(1-\Pi_{\rm L}^2)$ and μ. To keep the phases of $\Pi_{\rm V}$ and $\Pi_{\rm L}$ off by 180°, we need (iii) the sign of $g + \mu\Pi_{\rm V}$ and $g\Pi_{\rm V} + \mu(1-\Pi_{\rm L}^2)$ to be the same. As we see from bursts 779 and 926 in Figure 2, the phase differences between $\Pi_{\rm L}$ and $\Pi_{\rm V}$ are both close to 180° regardless of the sign of $\Pi_{\rm V}$. In this way, according to condition (iii), g should not be zero; otherwise, the phase between $\Pi_{\rm L}$ and $\Pi_{\rm V}$ depends on the sign of $\Pi_{\rm V}$. A nonzero value of g means

that Faraday conversion processes exist. Lacking detailed modeling, we cannot conclude whether the Faraday conversion is relativistic or nonrelativistic at this stage. We expect that future modeling may reveal more details on the magnetoionic environment close to the FRB emission site.

Besides Faraday conversion, polarisation-dependent scintillation can also induce such λ^2 oscillations in degree of polarisation[64]. However, special conditions are required to reproduce the reduction of oscillations in $\Pi_{\rm L}$ and $\Pi_{\rm V}$ above 1160 MHz for burst 779, the characteristic frequency of a uniformly magnetised plasma[63] may provide a natural mechanism. One expects that the Lorentz factor of the corresponding relativistic electrons is $\gamma = 15(f/{\rm GHz})^{1/2}({\rm B/G})^{-1/2}$. That is, an environment with mildly relativistic electrons and a Gauss-level magnetic field may provide the conditions for such polarisation oscillations.

The occurrence of oscillatory polarisation appears less frequently during the time window when RM is stable. Such a behaviour can be understood in the framework of nonrelativistic Faraday conversion, which requires the reversal of longitudinal magnetic fields. When RM is stable, one expects fewer field reversals, and so less Faraday conversion occurrence.

We note that not all bursts with the measured nonzero $\Pi_{\rm V}$ show the above oscillatory behaviour. Some bursts exhibit slow variations with opposite phases of $\Pi_{\rm V}$ and $\Pi_{\rm L}$, such as burst 1112 in Figure 2. The variation may come from Faraday conversion or an intrinsic radiation mechanism of FRBs. Interestingly, the burst with the highest $\Pi_{\rm V}$ in our sample (burst 1472 in Figure 2) shows no significant oscillation. Therefore, on top of Faraday conversion, an alternative, intrinsic radiation mechanism may be required to generate circular polarisation.

Keck optical and near-infrared observations

The LRIS [65,66] spectroscopic observations were taken with a slit width of $1.0''$ at a position angle ${\rm PA} = 53.4^\circ$, and there were $750 + 920$ s and 2×750 s exposures on the blue and red sides, respectively. LRIS has an atmospheric dispersion corrector. The data were reduced using LPipe [67], and the fluxes were scaled to match Pan-STARRS1 [68] $griz$ photometry. Galactic extinction corrections[69,70] were applied with $R_V = 3.1$ and $E(B-V)_{\rm MW} = 0.652$ mag. We took 8×320 s exposures with ESI[71] in the cross-dispersed echelle mode with resolving power $R \approx 10,000$ and a slit width of $1.0''$ at the parallactic angle [72] of PA $= 87^\circ$. They were reduced with ESIRedux [3] with only relative-flux calibration performed.

The LRIS imaging consisted of 4×180 s exposures in the g band and 2×180 s in the i band. They were reduced following standard procedures of bias subtraction, flat fielding, and coadding.

[3] https://www2.keck.hawaii.edu/inst/esi/ESIRedux/index.html

We obtained 4×120 s K'-band images (dithered by 3–4″ between exposures) with the NIRC2 camera ($0.04''$ pixel^{-1} scale and $40''$ field) via the Keck II laser guide-star AO system [73]. An $R = 15.9$ mag star $36''$ NW of the FRB host served as the tip-tilt reference star. The near-infrared images were reduced following a standard iterative procedure[4], and the final combined image reaches a FWHM resolution of $0.12''$. The astrometry is calibrated using the SDSS coordinates of bright unsaturated stars.

Properties of the foreground galaxy

Star-formation rate and gas-phase metallicity We use the emission lines detected in the high-S/N LRIS spectrum to infer the star-formation rate (SFR) and the gas-phase metallicity of the galaxy. We measure line fluxes of Hα, [N II]λ6548, [N II]λ6583, [O III]λ5007, [O II]$\lambda\lambda$3726, 3729, and [S II]$\lambda\lambda$6716, 6731 by fitting single-Gaussian profiles; for Hβ, we add an additional Lorentzian component to account for stellar absorption.

We use the Hα luminosity $L(\mathrm{H}\alpha)$ to estimate the SFR. The internal extinction inside the galaxy is estimated with the Balmer decrement by adopting $(\mathrm{H}\alpha/\mathrm{H}\beta)_{\mathrm{theory}} = 2.86$ for Case B recombination and using the Calzetti et al.[74] reddening curve; we obtain $E(B-V) = 0.43 \pm 0.04$ mag and thus $A_\lambda(\mathrm{H}\alpha) = 1.27 \pm 0.12$ mag, yielding $L(\mathrm{H}\alpha) = (6.9 \pm 0.7) \times 10^{41}$ erg s^{-1}, which translates to SFR $= 3.4 \pm 0.3\, M_\odot$ yr^{-1} by following ref.[75]. Our SFR estimate is higher than previous $L(\mathrm{H}\alpha)$-based measurements, $\approx 2.1\,\mathrm{M_\odot yr^{-1}}$ (ref. [10]), $\approx 1.7\,\mathrm{M_\odot yr^{-1}}$ (ref.[11]), and $2.3 \pm 0.4\,\mathrm{M_\odot yr^{-1}}$ (ref.[12]), while it is lower than those derived from SED fitting ($\approx 4.3\,\mathrm{M_\odot yr^{-1}}$[ref.[10]]) and radio data ($\approx 7\,\mathrm{M_\odot yr^{-1}}$[ref.[11]] and $\approx 10\,\mathrm{M_\odot yr^{-1}}$[ref.[12]]) Adopting a stellar mass $M_* = 2.5 \pm 0.7 \times 10^{10}\, M_\odot$ for the galaxy from averaging two existing results[10,11], the specific SFR is $\log(\mathrm{sSFR/yr^{-1}}) = -9.86 \pm 0.11$. We also cross-check it by estimating sSFR using EW(Hα) = 48Å and obtain $\log(\mathrm{sSFR/yr^{-1}}) = -9.65 \pm 0.19$ by following ref.[76], and it is higher than our $L(\mathrm{H}\alpha)$-based estimate by $\sim 1\,\sigma$.

We infer the gas-phase metallicity (Z) by applying the Inferring metallicities (Z) and Ionization parameters (q) (IZI) photoionisation model[77,78] to the fluxes of all the above-mentioned emission lines, yielding a best-fit oxygen abundance of 12 + log(O/H) = $9.07^{+0.03}_{-0.04}$, which is in agreement with a previous estimate [10] (12+log(O/H) = $9.03^{+0.15}_{-0.24}$) using the "O3N2" method.

Morphology and kinematic The left and middle subpanels of Extended Data Figure 7(a) show the LRIS i-band and the NIRC2 K-band AO images, respectively. The AO image with FWHM

[4] https://github.com/fuhaiastro/nirc2

$= 0.12''$ enables resolving the bar and spiral features of the galaxy, which is not possible with natural seeing. We used GALFIT [79] to model the host galaxy in the NIRC2 image with a single-component model composed of a Sérsic profile in the radial direction and a generalized ellipse function in the azimuthal direction. We obtain the best-fit effective radius $R_e = 1.5\,\mathrm{kpc}$ and axis ratio $b/a = 0.62$, which suggests cos (i) = 0.6 (where i is disk inclination angle) [80,81]. After subtracting the disk component, the galaxy bar and spiral features can be clearly seen in the residual NIRC2 image shown in the right-most subpanel of Extended Data Figure 7(a). We measure the centroid of the galaxy bar by fitting a 2D Gaussian model and obtain refined coordinates of the galaxy center (RA $= 05^{\mathrm{h}}08^{\mathrm{m}}03.484^{\mathrm{s}}$, Dec $= +26^{\circ}03'37.90''$). The FRB is $0.32 \pm 0.06''$ and $0.61 \pm 0.06''$ to the East and North of the galaxy center, respectively, and its apparent position is on the disk, while does not appear to coincide with any other visible structures.

As shown in Extended Data Figure 7(b), the Hα line in the ESI spectrum has a double-peaked profile with a peak-to-peak separation of $\sim 100\,\mathrm{km\,s^{-1}}$, which may be due to disk rotation; however, since the ESI slit was oriented along the minor axis of the galaxy, it may alternatively be caused by gas outflow. We study the disk rotation with LRIS, for which the slit was oriented 60° with respect to the major axis. As shown in the left subpanels of Extended Data Figure 7(c), the wavelength centroids of Hα emission vary along the LRIS slit direction. We extract Hα lines with a step size of 3 pixels ($0.4''$) along the slit direction, and we measure their projected galactocentric distance $r_{\perp}$ and line-of-sight velocities v to the continuum center shown as the black dots in the right subpanel of Extended Data Figure 7(c). Then we fit the data using a simple rotational disk model, in which velocity scales linearly with galactocentric distance r for $r < r_{\mathrm{break}}$ (the velocity zero point is a free parameter) and stays constant at v_{ROT} for $r > r_{\mathrm{break}}$. The best-fit model, which is shown as the red line in the right subpanel of Extended Data Figure 7(c), has the deprojected rotation velocity $v_{\mathrm{ROT}} = 139 \pm 19\,\mathrm{km\,s^{-1}}$ and $r_{\mathrm{break}} = 3.0 \pm 0.5\,\mathrm{kpc}$. Our v_{ROT} estimate suggests a galaxy stellar mass $M_* \approx 2 \times 10^{10}\,M_{\odot}$ using the Tully-Fisher relation [81,82]. This is consistent with our adopted value $M_* = 2.5 \pm 0.7 \times 10^{10}\,M_{\odot}$ from averaging two previous estimates [10,11].

Properties of the background galaxy

Fong et al.[10] tentatively identified a background galaxy with the possible detection of Hβ and [O III] emission lines at $z = 0.5531$. Our spectra allow its firm identification and study of its properties.

We detect Hα, Hβ, and [O III] $\lambda\lambda$4959, 5007 emission lines at $z = 0.5534 \pm 0.0001$ in the LRIS (blue) and ESI (cyan) spectra. Owing to the nondetection of [N II] (or [O II]), we cannot distinguish between a star-forming galaxy and an active galactic nucleus (AGN) in the BPT

diagram (see Extended Data Figure 8(a)). The [O III] $\lambda5007$ line is resolved by ESI with a velocity dispersion $\sigma_{[\mathrm{O\,III}]\lambda5007} = 27.6 \pm 2.6\,\mathrm{km\,s^{-1}}$; such a low velocity dispersion favors that it is a star-forming galaxy[83]. Using IZI, we find that its gas-phase metallicity 12 + log(O/H) = $8.29^{+0.26}_{-0.28}$ and $E(B-V) = 0.27^{+0.12}_{-0.13}$ mag. The extinction-corrected Hα luminosity is $L(\mathrm{H}\alpha) = 1.14^{+0.51}_{-0.38} \times 10^{42}\,\mathrm{erg\,s^{-1}}$, which yields SFR = $5.7^{+2.5}_{-1.9}\,M_\odot\,\mathrm{yr^{-1}}$.

As shown in the right sub-panels of Figure 3(b), the centers of [O III] $\lambda5007$ emission from the background galaxy are offset from the center of the continuum dominated by the foreground galaxy in the 2D spectroscopic image. We determine that the center of the background galaxy is $0.29''$ to the West and $0.22''$ to the North of foreground galaxy's center. Their angular proximity gives rise to an interesting possibility that the background galaxy might be gravitationally lensed by the foreground galaxy. Assuming a simple Singular Isothermal Sphere (SIS) model with $\sigma_v = v_{\mathrm{ROT}}/\sqrt{2} = 98\,\mathrm{km\,s^{-1}}$ for the foreground galaxy, the angular Einstein radius [84] can be estimated as $\theta_{\mathrm{E}} \approx 0.2''$. Further data and analysis will be required to verify lensing.

Simultaneous high-energy observations

Piro et al.[12] placed lower bounds for the radio-to-X-ray luminosity ratio of $\geq 2 \times 10^{-6}$ based on the null detection of the transient in *Swift*/XRT and *Chandra* data. We focus on γ-ray counterparts of the 1863 radio bursts using *Fermi*/GBM, *Insight*-HXMT, and GECAM, of which the observational sessions covered 1119, 1226, and 456 bursts, respectively. In total, 1708 radio bursts were covered by at least one instrument. The searching methods of Zou et al.[85] and Cai et al.[86] were used for *Fermi* and *Insight*-HXMT/GECAM data, respectively.

No significant transient with $S/N \geq 5$ was identified within 10 s windows centred on the radio burst. Assuming the same spectral parameters as observed in the FRB 200428-associated X-ray burst (ref.[6]), the 1 s 3σ upper limit of the energy flux in the 8–200 keV band from *Fermi*/GBM data is $8.1 \times 10^{-8}\,\mathrm{erg\,cm^{-2}\,s^{-1}}$, and the upper limits from GECAM and *Insight*-HXMT data are $4.2 \times 10^{-8}\,\mathrm{erg\,cm^{-2}\,s^{-1}}$ (15–200 keV) and $1.8 \times 10^{-8}\,\mathrm{erg\,cm^{-2}\,s^{-1}}$ (200–3000 keV), respectively. Accordingly, the ratio between the luminosity in radio and γ-ray bands, $L_{\mathrm{radio}}/L_\gamma$, is constrained at $\geq 1.4 \times 10^{-7}$ (8–200 keV), and $\geq 6.3 \times 10^{-7}$ (200–3000 keV).

Data availability

Raw data are available from the FAST data center: http://fast.bao.ac.cn. Owing to the large data volume, we encourage contacting the corresponding author for the data transfer. The directly related data that support the findings of this study can be found from PSRPKU website: https://psr.pku.edu.cn/index.php/publications/frb20201124a/.

Code availability

PSRCHIVE (http://psrchive.sourceforge.net)

TRANSIENTX (https://github.com/ypmen/TransientX)

BEAR (https://psr.pku.edu.cn/index.php/publications/frb180301/)

Acknowledgements This work made use of data from the FAST. FAST is a Chinese national mega-science facility, built and operated by the National Astronomical Observatories, Chinese Academy of Sciences. We acknowledge the use of public data from the Fermi Science Support Center (FSSC). This work is supported by National SKA Program of China (2020SKA0120100, 2020SKA0120200), Natural Science Foundation of China (12041304, 11873067, 11988101, 12041303, 11725313, 11725314, 11833003, 12003028, 12041306, 12103089, U2031209, U2038105, U1831207), National Program on Key Research and Development Project (2019YFA0405100, 2017YFA0402602 ,2018YFA0404204, 2016YFA0400801), Key Research Program of the CAS (QYZDJ-SSW-SLH021), Natural Science Foundation of Jiangsu Province (BK20211000), Cultivation Project for FAST Scientific Payoff and Research Achievement of CAMS-CAS, the Strategic Priority Research Program on Space Science, the Chinese Academy of Sciences (Grant No. XDA15360000, XDA15052700, XDB23040400), funding from the Max-Planck Partner Group, the science research grants from the China Manned Space Project (CMS-CSST-2021-B11,NO. CMS-CSST-2021-A11), and PKU development grant 7101502590. AVF's group at U.C. Berkeley is supported by the Christopher R. Redlich Fund, the Miller Institute for Basic Research in Science (in which A.V.F. is a Miller Senior Fellow), and many individual donors. SD acknowledges the support from the XPLORER PRIZE. BBZ acknowledges support by Fundamental Research Funds for the Central Universities (14380046), and the Program for Innovative Talents, Entrepreneur in Jiangsu. We thank the staff of W.M. Keck Observatory for their help during the observing runs. We thank L. Ho, H. Gao and R. Li for discussions.

Author Contributions HX, JRN, PC led the data analysis. KJL, WWZ, SD, and BZ coordinated the observational campaign, co-supervised data analyses and interpretations, and led the paper writing. JCJ conducted the polarisation and RM measurements. BJW, JWX, CFZ, KJL did the timing analysis, periodicity search, DM measurement, burst searching, and Faraday conversion measurement. YPM contribute to the searching software developing, and RNC, MZC, LFH, YXH,ZYL, ZXL, YHX, JPY performed software

testing. DJZ, YKZ,YF, CHN, FYW,XFW contributed to, radio data analysis. PC, SD, HF, AVF, EWP, TGB, SGD, PG, DS, AS, WKZ, and AE contributed to the optical observations and data reduction; AVF also edited the manuscript in detail. PC, SD, HF and YL contributed to analyzing and interpreting the optical data. PJ, HQG, JLH, JLH, HL,QL, JHS, RY, YLY, DJY, YZ aided with FAST observations. JLH, DL, MW, NW helped with observation coordination. KJL, BZ, DZL, WYW, RXX, WL,YPY,ZGD,RL provided theoretical discussions. CC, CKL, XQL, WXP, LMS, SX, SLX, JY, XY, QBY, BBZ, SNZ, JHZ contributed to the high energy observation.

Competing Interests The authors declare no competing financial interests.

Correspondence Requests for materials should be addressed to the following:
K. J. Lee (E-mail:kjlee@pku.edu.cn)
S. Dong (E-mail: dongsubo@pku.edu.cn)
W. W. Zhu (E-mail:zhuww@nao.cas.cn)
B. Zhang (Email:bing.zhang@unlv.edu)

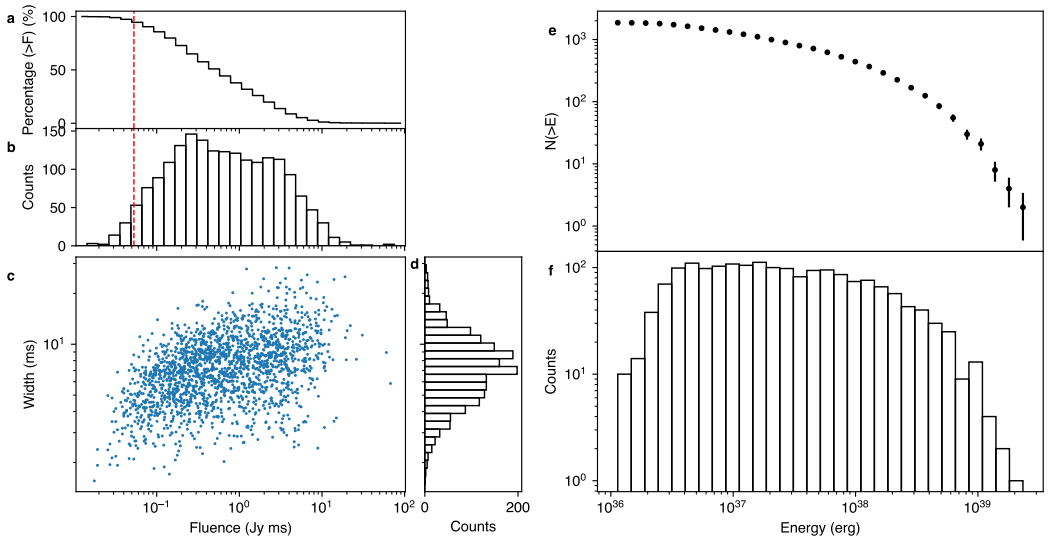

Extended Data Figure 1: **Fluence, equivalent width, and energy distribution for detected FRB 20201124A bursts.** (a) and (b) The cumulative distribution and the histogram of the burst fluence; the red dashed vertical line at 53 mJy ms indicates the completeness threshold of fluence at the 95% confidence level. (c) The 2D distribution of fluence and pulse width. (d) Histogram of pulse width. (e) and (f) Cumulative distribution and histogram of FRB 20201124A burst energy.

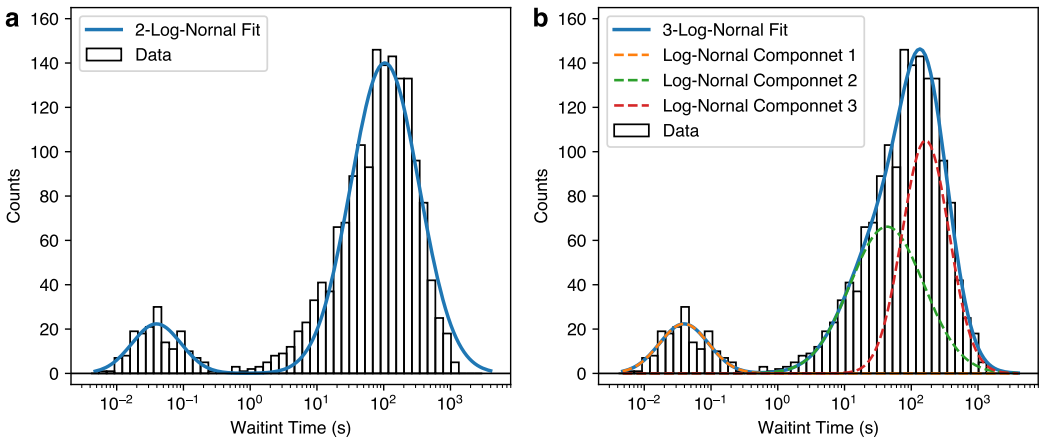

Extended Data Figure 2: **Waiting time distribution of FRB 20201124A.** The distribution of the waiting timescale as shown in the histogram. (a) The best fit using two log-normal functions to this distribution is shown by the blue curve, with the two log-normal distributions peaking at 39 ms and 106.7 s respectively. (b) The best fit (blue curve) using three log-normal functions peaking at 39 ms, 45.1 s, and 162.3 s.

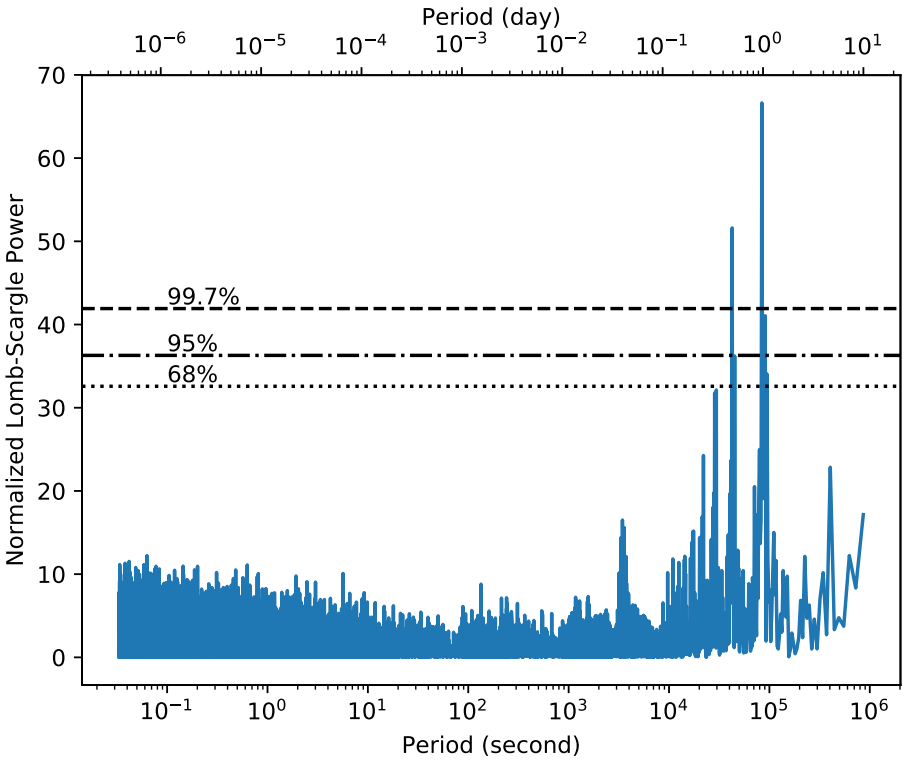

Extended Data Figure 3: **Lomb-Scargle periodogram of bursts for FRB 20201124A.** The period is searched in the range from 30 ms to 10 days, and the 68%, 95%, and 99.7% confidence limits are labeled with dashed, dashed-dotted, and dotted horizontal lines, respectively.

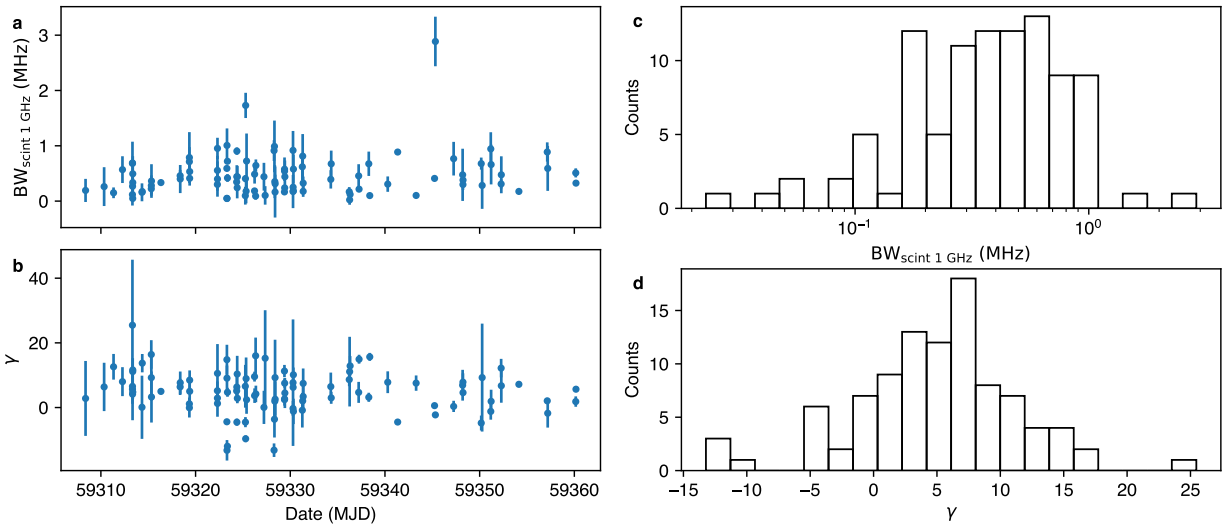

Extended Data Figure 4: **Scintillation measurements.** (a) The scintillation bandwidth measurement at a reference frequency of 1 GHz. (b) The best-fit power-law index to the scintillation bandwidth. (c) and (d) The relevant distributions.

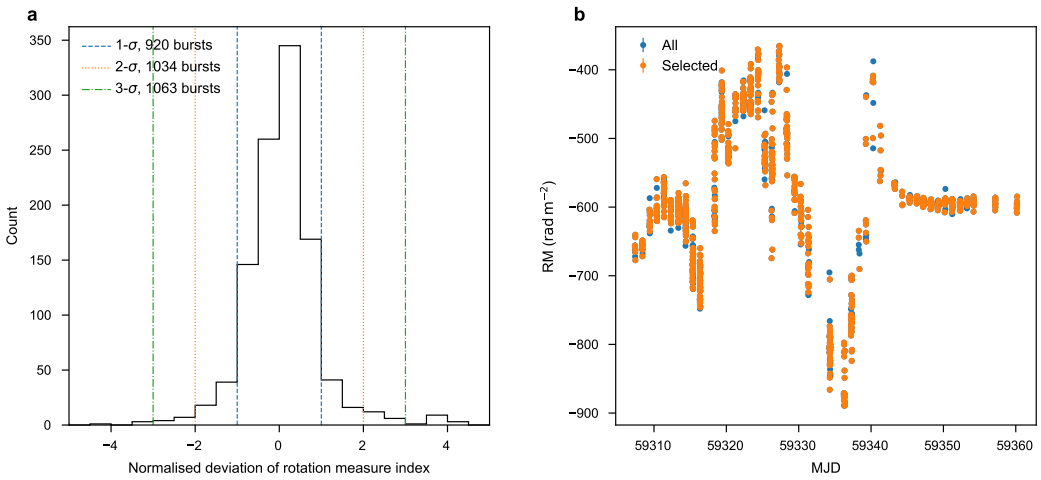

Extended Data Figure 5: **Rotation measure index.** (a) Histogram of normalised rotation measure index deviation defined as $(\beta - 2)/\sigma_\beta$. Here, rotation measure index β is defined from $\Delta\Psi = \mathrm{RM}\,\lambda^\beta$, and σ_β is the uncertainty of β with 68% confidence level computed from the Bayesian fitting. For a total of 1103 bursts, only 40 of them have beyond-3σ RM index deviation from 2. (b) Variations of all RMs (blue) and selected RMs (orange) whose normalised rotation measure index deviation is smaller than 1.

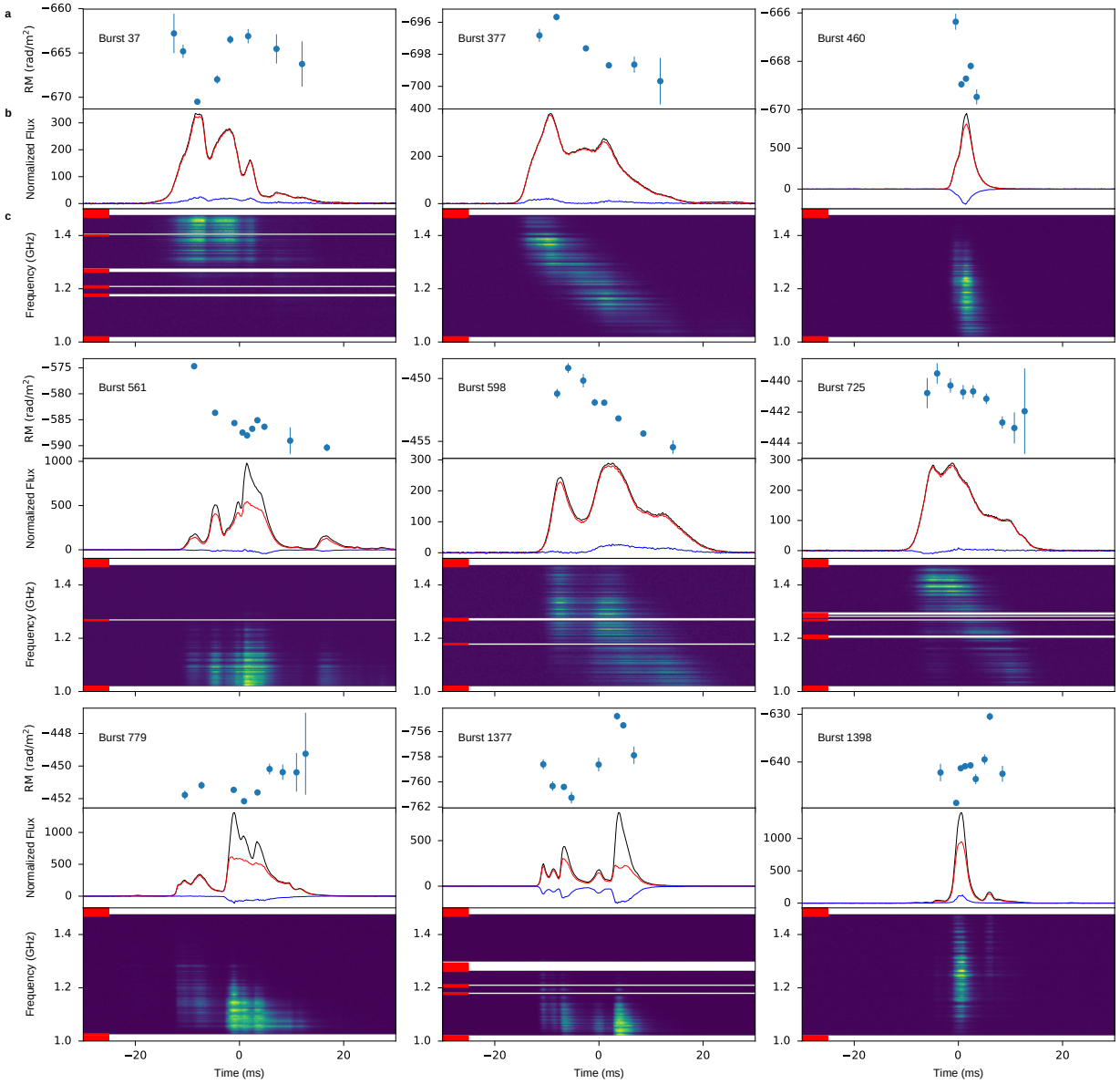

Extended Data Figure 6: **RM variation within individual bursts.** Nine bursts are presented. For each burst, (a) RM curve with 95% confidence level error bars. (b) and (c) The same as (b) and (c) in Figure 1, respectively. Bursts are dedispersed using corresponding structure-optimised DM values. The weighted RM value over burst phases from the best Bayesian RM values of each phase is used to derotate the linear PA for each burst. The pulse number is given in the top-left corner.

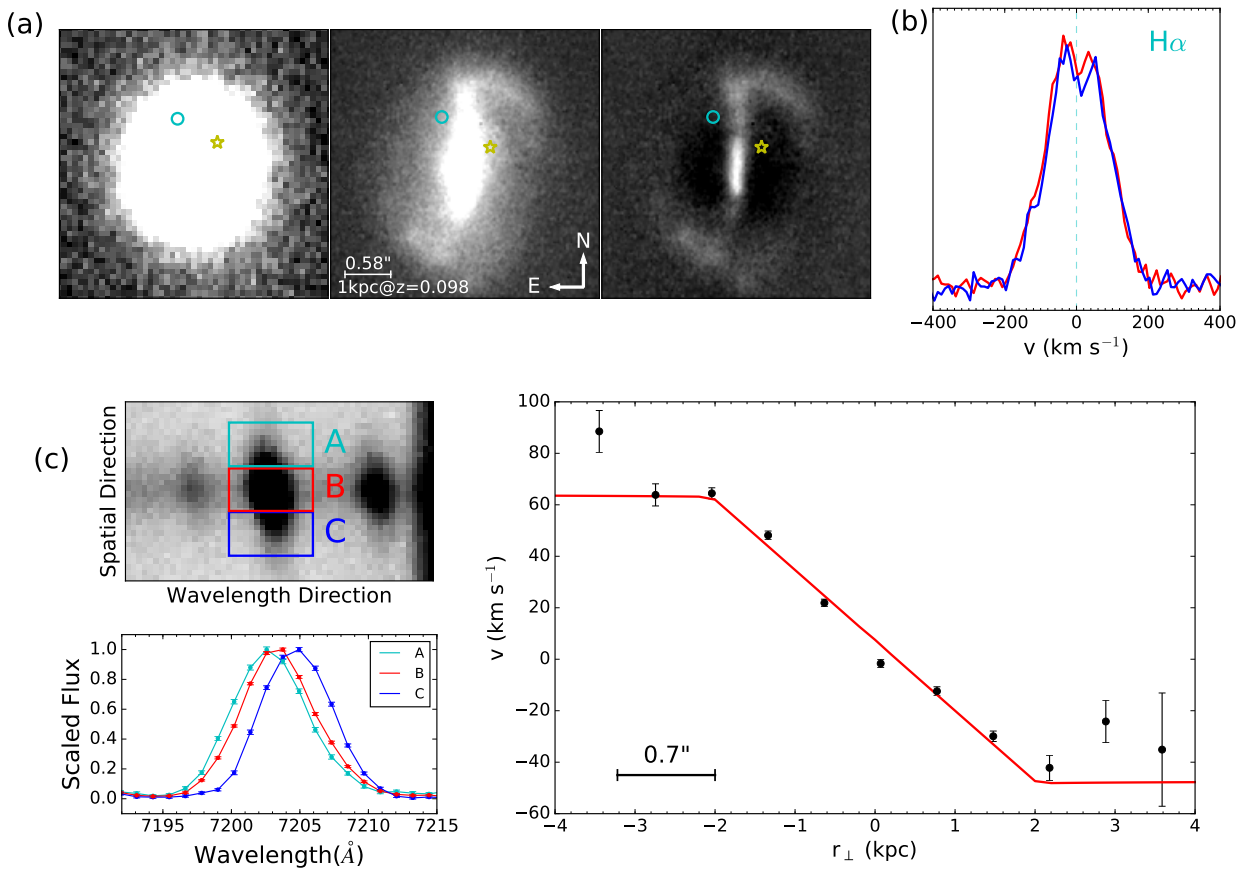

Extended Data Figure 7: **Properties of the foreground galaxy at $z = 0.098$ in the optical and near-infrared.** (a) Host-galaxy morphology. The left and middle panels show the i-band and K'-band images of the FRB 20201124A host galaxy taken with LRIS and NIRC2, respectively. The right panel shows the residual image after subtracting the disk component from the image in the middle panel. The three images have the same orientation and angular scale as shown in the middle panel. The EVN localisation of FRB 20201124A is indicated with the cyan circle, and the center of the background galaxy ($z = 0.553$) is shown as the yellow asterisk. (b) The Hα double-peaked profile revealed in the medium-resolution ESI spectrum. The Hα lines in blue and red colors are from two different orders of the echelle spectrum. (c) Kinematic properties. The upper-left panel shows the 2D spectroscopic image around Hα emission from the LRIS observation. A wavelength-dependent variation is clearly seen in the spatial direction. The bottom-left panel shows Hα lines extracted from three different regions (corresponding to the three rectangles in the upper-left panel) of the galaxy along the slit. The velocities at different projected distances in the slit direction relative to the continuum center are shown in the right panel, and the red line is the best-fit result of a simple rotation model as described in the text. Note that the LRIS spectroscopic observations were taken with seeing of $0.7''$ (black bar), which sets the spatial resolution.

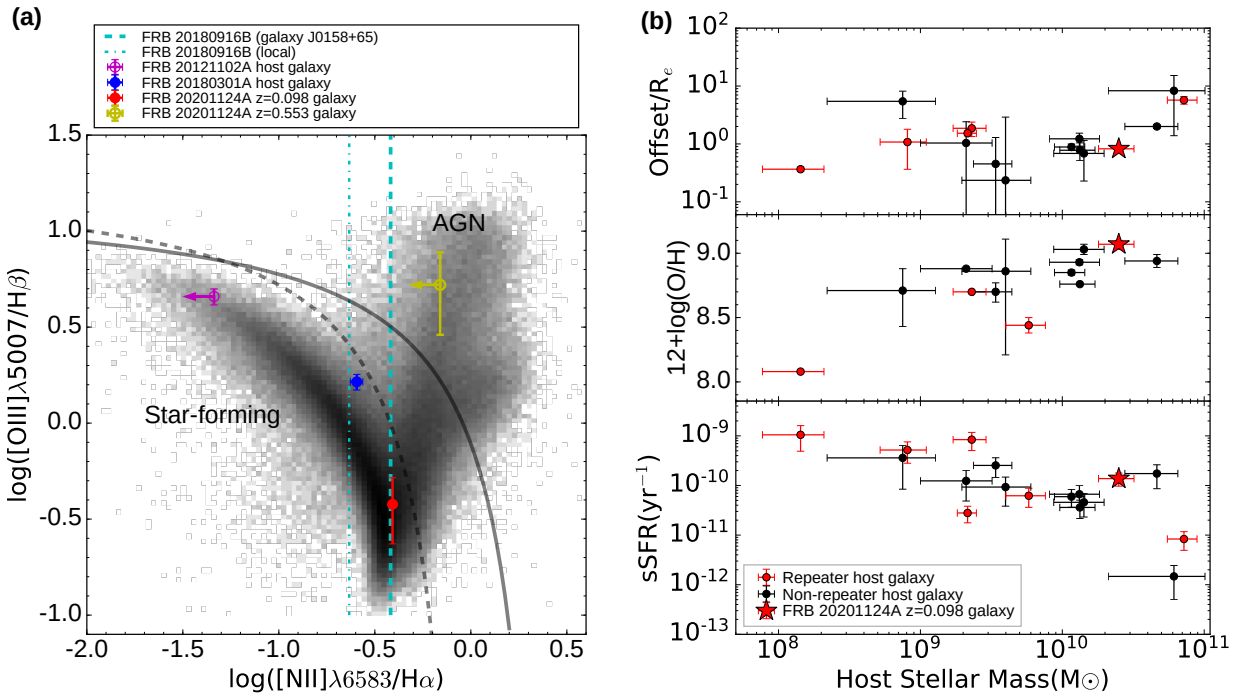

Extended Data Figure 8: **Host galaxy properties and comparisons with other FRB hosts** (a) FRB repeaters' hosts in the BPT diagram plotted with the SDSS DR8 MPA-JHU sample (black); galaxies dominated by star formation and active galactic nuclei are to the bottom left and upper right of the black dashed and solid lines[87,88], respectively. (b) The properties (FRB-galaxy offset in the units of galaxy effective radius R_e, gas-phase metallicity, sSFR, and stellar mass) of the FRB 20201124A $z = 0.098$ galaxy (red star) compared with a literature sample of FRB hosts (available at https://frbhosts.org/) shown with dots (black, nonrepeaters; red, repeaters).

35. Jiang, P. et al. The fundamental performance of FAST with 19-beam receiver at L band. Res. Astron. Astrophys. **20**, 064 (2020).

36. Men, Y. P. et al. Piggyback search for fast radio bursts using Nanshan 26 m and Kunming 40 m radio telescopes - I. Observing and data analysis systems, discovery of a mysterious peryton. Mon. Not. R. Astron. Soc. **488**, 3957–3971 (2019).

37. Oppermann, N., Yu, H.-R. & Pen, U.-L. On the non-Poissonian repetition pattern of FRB121102. Mon. Not. R. Astron. Soc. **475**, 5109–5115 (2018).

38. Feroz, F., Hobson, M. P. & Bridges, M. MULTINEST: an efficient and robust Bayesian inference tool for cosmology and particle physics. Mon. Not. R. Astron. Soc. **398**, 1601–1614 (2009).

39. Jenet, F. A. & Anderson, S. B. The Effects of Digitization on Nonstationary Stochastic Signals with Applications to Pulsar Signal Baseband Recording. Publ. Astron. Soc. Pac. **110**, 1467–1478 (1998).

40. Chime/Frb Collaboration et al. Periodic activity from a fast radio burst source. Nature **582**, 351–355 (2020).

41. Taylor, J. H. Pulsar Timing and Relativistic Gravity. Philos. Trans. Royal Soc. A **341**, 117–134 (1992).

42. Hobbs, G. B., Edwards, R. T. & Manchester, R. N. TEMPO2, a new pulsar-timing package - I. An overview. Mon. Not. R. Astron. Soc. **369**, 655–672 (2006).

43. Li, D. et al. A bimodal burst energy distribution of a repeating fast radio burst source. Nature **598**, 267–271 (2021).

44. Lomb, N. R. Least-Squares Frequency Analysis of Unequally Spaced Data. Astrophys. Space Sci. **39**, 447–462 (1976).

45. Hessels, J. W. T. et al. FRB 121102 Bursts Show Complex Time-Frequency Structure. Astrophys. J. Lett. **876**, L23 (2019).

46. Platts, E. et al. An analysis of the time-frequency structure of several bursts from FRB 121102 detected with MeerKAT. Mon. Not. R. Astron. Soc. **505**, 3041–3053 (2021).

47. Marthi, V. R. et al. Detection of 15 bursts from the fast radio burst 180916.J0158+65 with the upgraded Giant Metrewave Radio Telescope. Mon. Not. R. Astron. Soc. **499**, L16–L20 (2020).

48. Cordes, J. M., Weisberg, J. M. & Boriakoff, V. Small-scale electron density turbulence in the interstellar medium. Astrophys. J. **288**, 221–247 (1985).

49. Cordes, J. M., Pidwerbetsky, A. & Lovelace, R. V. E. Refractive and Diffractive Scattering in the Interstellar Medium. Astrophys. J. **310**, 737 (1986).

50. Cordes, J. M. & Lazio, T. J. W. NE2001.I. A New Model for the Galactic Distribution of Free Electrons and its Fluctuations. arXiv e-prints astro–ph/0207156 (2002). astro-ph/0207156.

51. Yao, J. M., Manchester, R. N. & Wang, N. A New Electron-density Model for Estimation of Pulsar and FRB Distances. Astrophys. J. **835**, 29 (2017).

52. Deng, W. & Zhang, B. Cosmological Implications of Fast Radio Burst/Gamma-Ray Burst Associations. Astrophys. J. Lett. **783**, L35 (2014).

53. Luo, R., Lee, K., Lorimer, D. R. & Zhang, B. On the normalized FRB luminosity function. Mon. Not. R. Astron. Soc. **481**, 2320–2337 (2018).

54. Dolag, K., Gaensler, B. M., Beck, A. M. & Beck, M. C. Constraints on the distribution and energetics of fast radio bursts using cosmological hydrodynamic simulations. Mon. Not. R. Astron. Soc. **451**, 4277–4289 (2015).

55. Hotan, A. W., van Straten, W. & Manchester, R. N. PSRCHIVE and PSRFITS: An Open Approach to Radio Pulsar Data Storage and Analysis. Publ. Astron. Soc. Aust. **21**, 302–309 (2004).

56. Desvignes, G. et al. Radio emission from a pulsar's magnetic pole revealed by general relativity. Science **365**, 1013–1017 (2019).

57. Sotomayor-Beltran, C. et al. Calibrating high-precision Faraday rotation measurements for LOFAR and the next generation of low-frequency radio telescopes. Astron. & Astrophys. **552**, A58 (2013).

58. Hilmarsson, G. H. et al. Rotation Measure Evolution of the Repeating Fast Radio Burst Source FRB 121102. Astrophys. J. Lett. **908**, L10 (2021).

59. Xu, J. & Han, J. L. Redshift evolution of extragalactic rotation measures. Mon. Not. R. Astron. Soc. **442**, 3329–3337 (2014).

60. Noutsos, A., Karastergiou, A., Kramer, M., Johnston, S. & Stappers, B. W. Phase-resolved Faraday rotation in pulsars. Mon. Not. R. Astron. Soc. **396**, 1559–1572 (2009).

61. Cho, H. et al. Spectropolarimetric Analysis of FRB 181112 at Microsecond Resolution: Implications for Fast Radio Burst Emission Mechanism. Astrophys. J. Lett. **891**, L38 (2020).

62. Sazonov, V. N. Generation and Transfer of Polarized Synchrotron Radiation. Soviet Ast. **13**, 396 (1969).

63. Huang, L. & Shcherbakov, R. V. Faraday conversion and rotation in uniformly magnetized relativistic plasmas. Mon. Not. R. Astron. Soc. **416**, 2574–2592 (2011).

64. Beniamini, P., Kumar, P. & Narayan, R. Faraday depolarization by multi-path propagation and application to FRBs. arXiv e-prints arXiv:2110.00028 (2021).

65. Oke, J. B. et al. The Keck Low-Resolution Imaging Spectrometer. Publ. Astron. Soc. Pac. **107**, 375 (1995).

66. Rockosi, C. et al. The low-resolution imaging spectrograph red channel CCD upgrade: fully depleted, high-resistivity CCDs for Keck. In McLean, I. S., Ramsay, S. K. & Takami, H. (eds.) Ground-based and Airborne Instrumentation for Astronomy III, vol. 7735 of Society of Photo-Optical Instrumentation Engineers (SPIE) Conference Series, 77350R (2010).

67. Perley, D. A. Fully Automated Reduction of Longslit Spectroscopy with the Low Resolution Imaging Spectrometer at the Keck Observatory. Publ. Astron. Soc. Pac. **131**, 084503 (2019).

68. Flewelling, H. A. et al. The Pan-STARRS1 Database and Data Products. Astrophys. J., Suppl. Ser. **251**, 7 (2020).

69. Cardelli, J. A., Clayton, G. C. & Mathis, J. S. The Relationship between Infrared, Optical, and Ultraviolet Extinction. Astrophys. J. **345**, 245 (1989).

70. Schlafly, E. F. & Finkbeiner, D. P. Measuring Reddening with Sloan Digital Sky Survey Stellar Spectra and Recalibrating SFD. Astrophys. J. **737**, 103 (2011).

71. Sheinis, A. I. et al. ESI, a New Keck Observatory Echellette Spectrograph and Imager. Publ. Astron. Soc. Pac. **114**, 851–865 (2002).

72. Filippenko, A. V. The importance of atmospheric differential refraction in spectrophotometry. Publ. Astron. Soc. Pac. **94**, 715–721 (1982).

73. Wizinowich, P. L. et al. The W. M. Keck Observatory Laser Guide Star Adaptive Optics System: Overview. Publ. Astron. Soc. Pac. **118**, 297–309 (2006).

74. Calzetti, D. et al. The Dust Content and Opacity of Actively Star-forming Galaxies. Astrophys. J. **533**, 682–695 (2000).

75. Heintz, K. E. et al. Host Galaxy Properties and Offset Distributions of Fast Radio Bursts: Implications for Their Progenitors. Astrophys. J. **903**, 152 (2020).

76. Belfiore, F. et al. SDSS IV MaNGA - sSFR profiles and the slow quenching of discs in green valley galaxies. Mon. Not. R. Astron. Soc. **477**, 3014–3029 (2018).

77. Blanc, G. A., Kewley, L., Vogt, F. P. A. & Dopita, M. A. IZI: Inferring the Gas Phase Metallicity (Z) and Ionization Parameter (q) of Ionized Nebulae Using Bayesian Statistics. Astrophys. J. **798**, 99 (2015).

78. Mingozzi, M. et al. SDSS IV MaNGA: Metallicity and ionisation parameter in local star-forming galaxies from Bayesian fitting to photoionisation models. Astron. Astrophys. **636**, A42 (2020).

79. Peng, C. Y., Ho, L. C., Impey, C. D. & Rix, H.-W. Detailed Decomposition of Galaxy Images. II. Beyond Axisymmetric Models. Astron. J. **139**, 2097–2129 (2010).

80. Holmberg, E. A photographic photometry of extragalactic nebulae. Meddelanden fran Lunds Astronomiska Observatorium Serie II **136**, 1 (1958).

81. Tully, R. B. & Fisher, J. R. Reprint of 1977A&A....54..661T. A new method of determining distance to galaxies. Astron. & Astrophys. **500**, 105–117 (1977).

82. Ouellette, N. N. Q. et al. The Spectroscopy and H-band Imaging of Virgo Cluster Galaxies (SHIVir) Survey: Scaling Relations and the Stellar-to-total Mass Relation. Astrophys. J. **843**, 74 (2017).

83. Law, D. R. et al. SDSS-IV MaNGA: Refining Strong Line Diagnostic Classifications Using Spatially Resolved Gas Dynamics. Astrophys. J. **915**, 35 (2021).

84. Narayan, R. & Bartelmann, M. Lectures on Gravitational Lensing. arXiv e-prints astro–ph/9606001 (1996).

85. Zou, J.-H. et al. Periodicity Search on X-ray Bursts of SGR J1935+2154 Using 8.5-year Fermi/GBM Data. arXiv e-prints arXiv:2107.03800 (2021).

86. Cai, C. et al. Search for gamma-ray bursts and gravitational wave electromagnetic counterparts with High Energy X-ray Telescope of Insight-HXMT. Mon. Not. R. Astron. Soc. **508**, 3910–3920 (2021).

87. Kewley, L. J., Dopita, M. A., Sutherland, R. S., Heisler, C. A. & Trevena, J. Theoretical Modeling of Starburst Galaxies. Astrophys. J. **556**, 121–140 (2001).

88. Kauffmann, G. et al. The host galaxies of active galactic nuclei. Mon. Not. R. Astron. Soc. **346**, 1055–1077 (2003).